Journal of Nepal Geological Society, 2024, Vol. 67, pp. 107–126
https://doi.org/10.3126/jngs.v67i1.74590

Superposed remanent magnetization and magnetic fabric in Triassic carbonates of Tethys Himalaya (Jomsom area, Nepal): chronological and tectonic implications

***Pitambar Gautam[1,2], Kohki Yoshida[3], Megh Raj Dhital[4], Shigeyuki Suzuki[5], Toshio Kawamura[6] and Babu Ram Gyawali[7,8]**

[1]*The Hokkaido University Museum, Hokkaido University, N10W8, Hokkaido 010-0810, Sapporo, Japan*
[2]*Creative Research Institution, Hokkaido University, N21W10, Kita-ku, Hokkaido 001-0021, Sapporo, Japan.*
[3]*Department of Geology, Faculty of Science, Shinshu University, Matsumoto, 390-8621, Japan*
[4]*Central Department of Geology, Tribhuvan University, Kirtipur, Kathmandu, Nepal*
[5]*Department of Earth Science, Okayama University, Okayama, 700-8530, Japan*
[6]*Department of Earth Science, Miyagi University of Education, Sendai, 980-0845, Japan*
[7]*Lumbini Engineering, Management and Science College, Pokhara University, Rupandehi, Nepal*
[8]*Institute of Fundamental Research and Studies, Kathmandu, Nepal*
**Corresponding author's email: pgautam@museum.hokudai.ac.jp, pitambargautam@yahoo.co.jp*

ABSTRACT

Carbonates from three sections in Tamba Kurkur and Mukut Formations near Jomsom in Nepal were investigated for natural remanent magnetization (NRM) and anisotropy of magnetic susceptibility (AMS). NRM comprises up to three components: a recent field component (RF) residing on magnetite/maghemite (soft coercivity: <10-15 mT) and goethite (low unblocking temperature range (T_{ub}): <150°C), a pyrrhotite-based characteristic remanence (ChRMpyr; intermediate T_{ub}: 180-350°C); and another based on magnetite (ChRMmag; high T_{ub}: 400-600°C). *In situ* ChRMpyr, with northerly declination and steep downward inclination (average value: 58.2°, steeper than the RF (48°) by 8-13°), is linked to thermochemical processes caused by low-temperature metamorphism at or after ca. 30 Ma. Mean CHRMpyr is steeper than the expected inclination by 24°, implying to post-acquisition tilting. Bedding-tilt corrected ChRMmag from Tamba Kurkur Formation is considered primary because of (i) steep negative inclination (-54.1°) implying acquisition at ca. 35°S latitude during the Triassic, and (ii) similarity to the known primary directions from Jomsom and adjacent areas (e.g., Manang, Shiar, Dolpo). Carbonates exhibit low mean magnetic susceptibility (k_m = 0.7-25.8×10^{-8} m^3kg^{-1}) contributed by diamagnetic and paramagnetic minerals. Magnetic fabric with low degree of anisotropy (P_J <1.12) and diverse ellipsoid shapes (-0.89 < T < 0.92) is a composite of several directional patterns. Discrimination of AMS data by specific ranges of scalar parameters (k_m, P_J and T) and comparison with mesoscopic structures reveals patterns linked to sedimentary-compaction, metamorphic and tectonic processes/phases.

Keywords: Magnetic Fabric; Magnetic Susceptibility; Carbonates; Pyrrhotite; Secondary Magnetization; Tethys Himalaya; Triassic

Received: 11 March 2024 **Accepted:** 2 October 2024

INTRODUCTION

The Himalayas together with the southern plains comprise essentially longitudinal geotectonic zones distributed from south to north, respectively, as the Indo-Gangetic Plain, Sub Himalaya, Lesser Himalaya, Higher Himalaya, and Tethys Himalaya (Fig. 1). Three master thrusts (Main Central Thrust (MCT), Main Boundary Thrust (MBT) and Main Frontal Thrust (MFT)), whose age of initiation becomes younger from north to south, separate the first four geotectonic zones, and come together at depth in a flat-lying decollement called the Main Himalayan Thrust (MHT) (Upreti 1999). The Tethys Himalaya is represented by Cambrian to Cretaceous-Eocene fossiliferous sedimentary rocks overlying the crystalline rocks of the Higher Himalaya along the South Tibetan Detachment System (STDS) that comprises a series of north dipping normal faults (Dhital 2015).

Tethys Himalaya, comprising marine sediments deposited within an ocean that once stretched across part of Eurasia, mainly occupies the Himalayan northern margin or the southern periphery of Tibet. Within Nepal, Tethys sediments occur between the Mahakali River and Tinkar Lipu on the west to Langtang Himal eastwards and further east in the Everest region. A few isolated remnants of these rocks occur within the Lesser Himalaya, whereas some synformally folded odd outliers cap the Higher Himalayan succession (e.g., in the vicinity of Kathmandu). The fossiliferous Tethyan realm attracted many geologists (e.g., Hagen 1968; Fuchs 1977; Bordet et al. 1971; Colchen et al. 1986; Dhital 2015), who established the basic geology supported by regional-scale maps, well-documented traverses and sections, and stratigraphy constrained by fossils. This subsequently paved the base for specialized and cross-disciplinary geoscience studies such as paleogeographic reconstructions (Gradstein et al., 1989,1991; von Rad et al. 1994; Ogg et al. 1994), thermo-chronometry (Garzanti et al. 1994a,b; Crouzet et al. 2007), structural mapping and tectono-

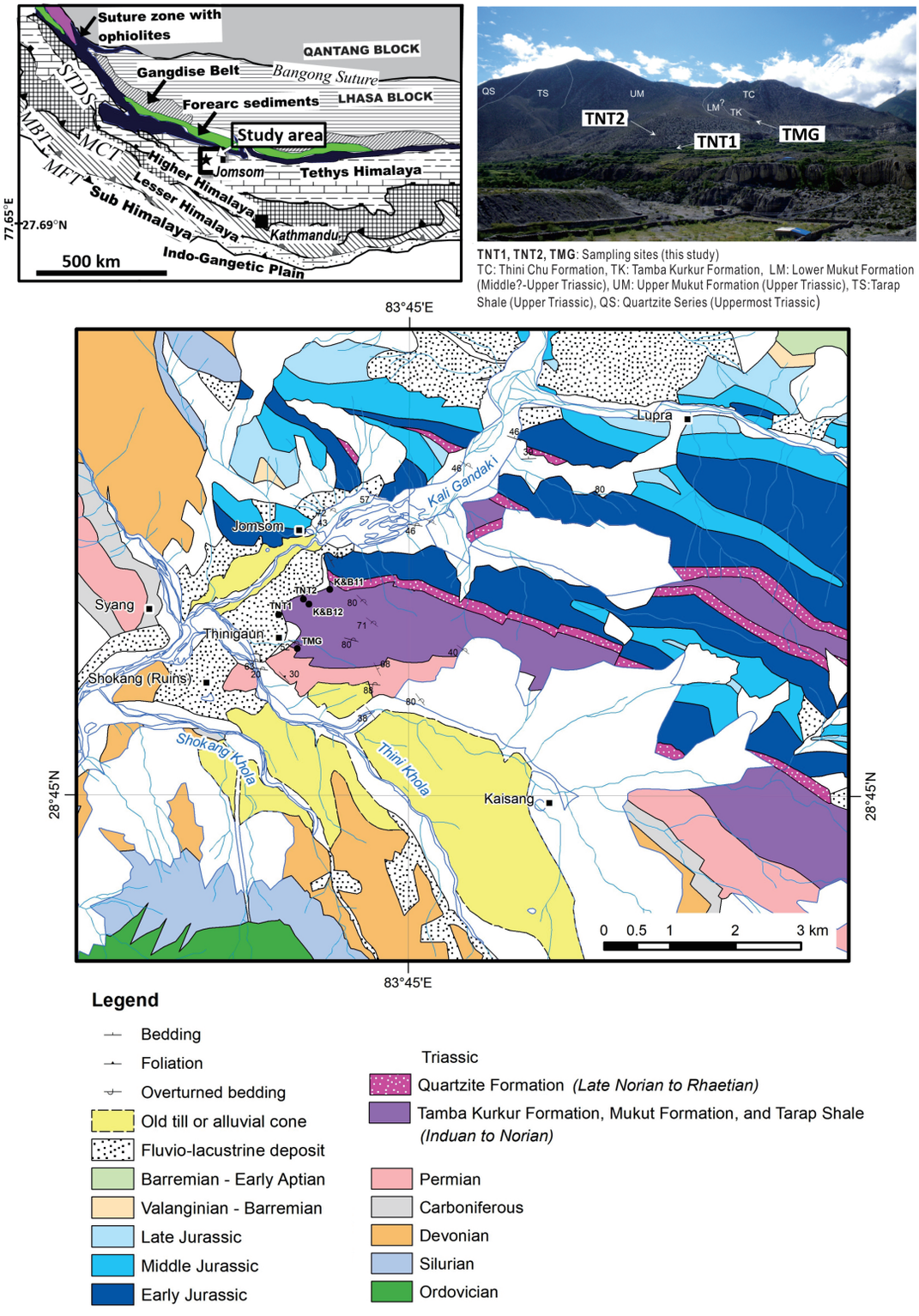

Fig. 1: Top left: Index map showing the major geological units surrounding the study area in central part of the Himalayas and a part of Tibet. A rectangle marks the study area in Tethys Himalaya near Jomsom (marked by a star) in north central Nepal. Major thrusts separating the major Himalayan Units are abbreviated as follows: MFT = Main Frontal Thrust, MBT = Main Boundary Thrust, MCT = Main Central Thrust, STDS = Southern Tibet Detachment System. Top right: Photograph showing the view to the NE of Jomsom with geological units and sampled sections (TMG, TNT1, TNT2). Bottom: Geological map of the study area after Dhital (2015) and new field observations, with locations of Triassic sections: TMG, TNT1, TNT2 (this paper) and KandB11, KandB12 (Klootwijk and Bingham 1980).

metamorphic studies (Carosi et al. 2007; Godin 2003; Kellet and Godin 2009; Montomoli et al. 2008), and paleomagnetic reconstructions (Klootwijk and Bingham 1980; Appel et al. 1991,2012; Schill et al. 2002a-c,2003,2004).

This study deals with magnetic properties of Triassic carbonates exposed near Jomsom (Fig. 1) to aid reconstruction of the geological past in the northern margin of the Neo-Tethys sea using environmental proxies (Suzuki et al. 2010; Yoshida et al. 2014). Remanent magnetization of these carbonates, together with sandstones covering Devono-Carboniferous to Early Cretaceous age, was partly studied by Klootwijk and Bingham (1980) revealing up to five remanence components: primary (depositional), secondary (collisional, metamorphic, and MCT-related), and recent field origin. The primary and secondary remanences were used to test different tectonic models involving the rotational underthrusting of the Indian Plate beneath Tibet, and to derive estimates for the northern extent of the former. This study focuses on short 10-25 m thick carbonate sections aiming at several objectives: (i) to explore the possibility to construct polarity stratigraphy for accurate dating; (ii) to determine the remanence-carrying magnetic minerals; (iii) to explore the secondary remanence based on pyrrhotite found to be ubiquitous in the Tethyan domain in adjacent areas (e.g., Dolpo, Manang) (Appel et al. 2012 and references therein); and (iv) to establish the magnetic fabric and explore its potential use as an aid to study petrofabric, especially the microscale structures associated with tectono-metamorphic and deformation events (Schill et al. 2003; Parsons et al. 2016).

GEOLOGICAL AND TECTONIC BACKGROUND

Brief geological outline

The Jomsom area lies within the Thakkhola Graben, which represents the central tectonic domain of the Dolpo-Manang Synclinorium, a nearly 200 km long structure formed as a consequence of the collision between India and Asia in the Early Tertiary. Successive sequences from the Permian (Thini Chu Formation) to the Upper Triassic (Tarap shale) and Jurassic (Jomsom Limestone) occur near Jomsom. The Triassic Tamba Kurkur Formation comprises five subunits (Krystyn 1982; von Rad et al. 1994), with the lower part (i.e., subunits 1 and 2) of Griesbachian-Dienerian-partly Smithian and the upper part of Smithian to Spathian in age. The odd-numbered subunits represent a condensed sequence of deep (bathyal) carbonate environments far from terrigenous influx, and the practically quartz-free micritic limestone was formed in lesser water depths (several hundred meters) (Garzanti et al. 1992; Dhital 2015). Sedimentary rocks constituting Mukut Formation and Tarap Shale crop out to the east of Jomsom at an elevation of 3,100–3,400 m. The almost E-W striking strata typically exhibit steep dips to the north, with most beds overturned. A gradual change in lithology, from the Tamba Kurkur to Lower Mukut Formations, is observed at the mountain ridge situated east of the Thini village. The Lower Mukut Formation, ca. 50 m thick, consists mainly of alternating beds of intensely bioturbated sandy mudstone and marly limestone. The mudstone beds, comprising fine siltstone with coarse silt and very fine sand-sized grains, contain fossils, such as ammonoids, brachiopods, bryozoans, and foraminifers. The lower part exhibits alternation of intervals of black and gray colored limestone and mudstone represented by sandy siltstone and sandy mudstone. It is dominated by mudstone, with a few thin limestone beds at the base. The Upper Mukut Formation has a total thickness of ca. 600 m. The mudstone intervals, alternating with marly limestone, are made of sandy siltstone with fine to medium-sized quartz grains. Both siltstone and limestone intervals show large burrows of fossils. The marly limestone in the lower part shows wavy bedding, while laminated marly limestone in the upper part of the formation exhibit hummocky cross-stratification, diagnostic of surface storm activity. Small- and medium-scale folding and faulting resulting in stratigraphic repetitions and gaps make difficult ascertaining the stratigraphic continuity at several levels, including at the boundary horizon between the Tamba Kurkur Formation and Mukut Formation.

Tectono-metamorphic and deformation events

The entire Tethys Himalaya sequence was affected by folding and imbricate thrusting during four major tectonic stages: (i) The first and major Eohimalayan tectonic deformation phase (D1), prominent in the south, associated with the Middle Eocene to Late Oligocene India-Asia collision and characterized by top-to-the-south thrust faults and south-vergent folds (F1) with related axial plane foliation S1 (Hodges 2000; Burg and Chen 1984; Ratschbacher et al. 1994; Carosi et al. 2007; Aikman et al. 2008; Montomoli et al. 2008); (ii) The second Neohimalayan deformation phase (D2) characterized by F2 folds and related S2 axial plane cleavage (Carosi et al. 2007; Montomoli et al. 2008; Kellett and Godin 2009). From crosscutting relationships of structural elements and U-Pb geochronology, and c. 30-25 Ma dated K-Ar ages of newly formed illite, an Oligocene age is suggested for the D2 phase (Godin 2003; Crouzet et al. 2007); (iii) The D3 phase marked by synchronic activities of STDS and the MCT along the Himalayan arc leading to the exhumation of mid-crustal rocks during c. 23-17 Ma (Godin et al. 2006). Possibility of younger dates is suggested for the activity of STDS (e.g., 12.5 Ma for Khula Kangri granite: Edwards and Harrison 1997) and displacement along MCT (e.g., ca. 10 Ma in Arunachal: Yin 2006); (iv) The D4 phase remaining active during Miocene times when an orogen parallel (E-W) extension triggered NS-trending normal faults forming grabens that crosscut the Lhasa block and the Tethys Himalaya (Coleman 1996).

At regional and local scales, the imprints of tectono-metamorphic and deformation events vary depending on local structures, lithology, and the proximity to leucogranites and thrusts or faults. Garzanti et al. (1994a,b) carried out thermo-chronometric studies of three distinct tectonic domains of the Dolpo-Manang Synclinorium using illite crystallinity (IC), chlorite crystallinity (CC), vitrinite reflectance (Ro%) and conodont alteration index (CAI), and textural mineralogical changes in thin sections to discriminate various zones influenced by diagenesis and metamorphism. They found metamorphism much weaker in Thakkhola Graben (than in the adjacent Dolpo and Manang) in Mesozoic strata affected by only a strong diagenetic overprint attesting to detrital inheritance with only weak post-depositional heating. Their inferences are based on samples from Jomsom and Thini showing characteristics of zones (1-2) indicative of incipient to very weak migration of quartz boundaries, calcite occurring as micrite/microsparite, phyllosilicates occurring as mixed

layers to illite-chlorite, presence of glaucony/stipnomelane, and non-to very weak fabric alignment, where the matrix is altered to illite-chlorite. Based on the average ranges (IC:1.00-0.42, CC: 0.40-0.25; mean Ro%: 2.1-4.3, and CAI of 4.5 (with 20 myrs heating duration assumed)), the metamorphic temperatures were estimated to be 225-275°C. Occurrence of very low grade metasediments below the graben is attributed to large difference in sediment thickness removed from different parts of the synclinorium (10 kilometers from both Dolpo and Manang after peak metamorphism, instead of just 8 km from above Thakkhola) before the graben formation in the Late Neogene, when very low grade metasediments on its shoulders were downthrown and now lie buried at a depth of several kilometers (Garzanti et al. 1994).

SAMPLING AND LABORATORY PROCEDURE

Carbonates of Triassic age were sampled from short sections (TMG, TNT1, TNT2) for remanent magnetization (RM) and anisotropy of magnetic susceptibility (AMS) measurements (Fig. 1, 2). One or more cores (2.54 cm in diameter) obtained after drilling into the rock exposure using a portable gasoline engine and oriented with a magnetic compass were collected from several stratigraphic levels at each section. The TMG section (Lower Triassic, 17 sampling levels), belonging the Tamba Kurkur Formation, is exposed in a small cliff on the mountain slope. The carbonate rocks, alternating with thinly laminated mudstones ranging in grain size from clay to fine silt, are relatively fresh compared to other sections, and constitute a stratigraphically completely overturned structure. The TNT1 section (Middle Triassic, 15 sampling levels) is situated within the corn field, and it is predominated by lithofacies comprising mudstone-rich layers alternating with subordinate limestone beds. The sampled interval corresponds to the lower part (stratigraphic height: ca. 80-100 m) of the Upper Mukut Formation. The geological structure is monoclinal and moderately fresh samples show signs of intrusions by secondary veinlets. The TNT2 section (Middle Triassic; 10 sampling levels) has fresh to slightly weathered rocks exposed at the roadside. Its beginning corresponds to ca. 200 m stratigraphic height of the Upper Mukut Formation.

In the laboratory, each field-drilled core was cut into several standard specimens of ca. 2.2 cm length for paleomagnetic and rockmagnetic studies. Measurements of natural and induced remanences and demagnetization were made with a variety of instruments: a 760R U-channel pass-through Superconducting Magnetometer (2G Enterprizes) equipped with alternating field demagnetization (AFD) up to 80 mT; a TDS-1 thermal demagnetizer (Natsuhara-Giken) with residual field at the sample space of less than 10 nT), a KLY-3S kappabridge (AGICO) for measuring the low-field MS; a MMPM10 pulse magnetiser (Magnetic Measurements) and a SMD-88 spinner magnetometer (Natsuhara-Giken) to stepwise magnetize and measure isothermal remanent magnetization (IRM), and a NMB-89 magnetic balance (Natsuhara-Giken) to obtain

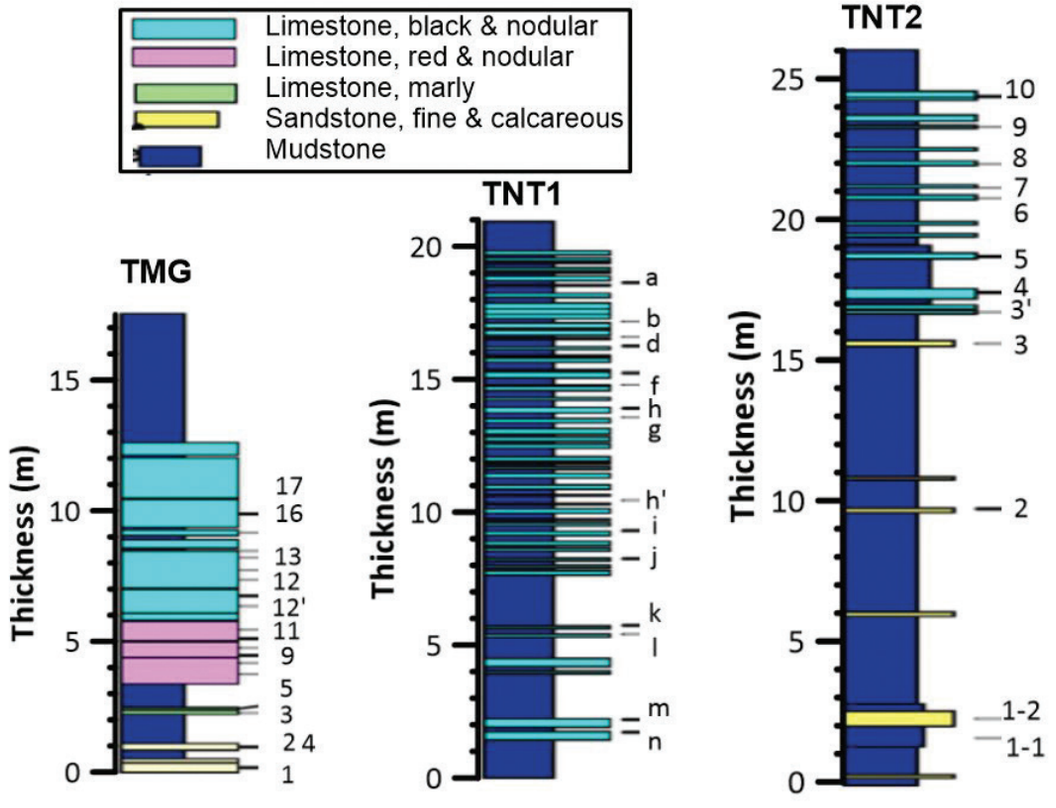

Fig. 2: Simplified lithologs of three sections (locations shown in Fig. 1) with sampling levels (with respect to the local base of the measured section) for magnetic measurements. The TMG section, located mid-slope, is a part if the Tamba Kurkur Formation (Lower Triassic). Sections TNT1 and TNT2, constituting the Upper Mukut Formation, begin at ca. 80-100m and ca. 200m above the base of the Mukut Formation (Middle Triassic).

thermomagnetic (high-field saturation magnetization (Js) versus temperature) curves for small amounts of samples in argon atmosphere. Measurements were carried out at the paleomagnetic laboratory of the Kochi Core Center, Japan. Demagnetization data were analyzed using PALMAG (Munich University) and puffinplot v2.2 (Lurcock and Wilson, 2012) softwares that enable principal component analysis (PCA, Kirschvink 1980). IRM analysis with the Gaussian technique for decomposition into lognormal distribution components based on mineral specific parameters (median acquisition fields ($B_{1/2}$) and half-width of the logarithmic dispersion parameter (DP) related to remanence coercivity followed Kruiver et al. (2001). Thermomagnetic curves were plotted using the MagePlot/MB online routine (Hatakeyama 2018). MS values measured in 15 different positions (following Jelinek's scheme) with KLY-3s were used to calculate susceptibility tensor elements used to characterize the magnetic fabric. Interactive AMS data processing and plotting directional data were performed using the Anisoft5 software (Chadima 2018).

MAGNETIC MINERALOGY AND REMANENT MAGNETIZATION

Magnetic mineralogy

IRM acquisition and decomposition

IRM acquisition curves and modelling data for three representative specimens, one from each section, comprising four components with distinct $B_{1/2}$, i.e., Comp1 (ca. 30 mT), Comp2 (76-89 mT), Comp3 (288-316 mT) and Comp4 (>1400 mT) are shown in Fig. 3 and Table 1. DP determined from the gradient is broad (0.35) for Comp1, whereas for others it lies within the 0.15-0.25 range. Comp1 is related to magnetite (soft coercivity), comp3 to pyrrhotite (intermediate coercivity), and comp4 to goethite (very hard coercivity), respectively (Peters and Dekkers 2003; Crouzet et al. 2003; Gautam et al. 2012). Magnetite may be of primary detrital as well as authigenic origin, while it might have variably converted to maghemite (a cation-deficient oxide mineral with spinel structure produced owing to low-temperature oxidation and pyrrhotite (produced thermo-chemically in presence of pyrite (Dunlop and Özdemir 1997; Crerar et al. 1978) in metasediments. Goethite, an iron hydroxide, was most probably formed under surficial weathering conditions (Schwertmann 1988). Goethite is common in these carbonates judging from the occurrences of a few cm thin limonitic layer (base of the Tamba Kurkur Formation), conspicuous ferruginous weathering, and yellow-brown and ochre colors (Mukut Formation) known from Dolpo (Fuchs 1973,1977).

Comp2 (with coercivity higher than that of comp1) contributing substantially to the isothermal remanence is inferred to reside on maghemite, whose presence is indicated also by notable decrease in NRM during initial AFD steps as well as by 400°C during ThD (section 4.2.1). Maghemite, a low-temperature oxidation or weathering product of magnetite, is capable of carrying a (thermo-)chemical remanence. It is metastable upon heating leading to transformation to weakly magnetic rhombohedral hematite above 250°C (Dunlop and Özdemir 1997, p. 58). Pyrrhotite, with a wide $B_{1/2}$ range (2.30-2.80) and distributed T_{ub} of 180-330°C, is known to be a strong carrier of (thermo-)chemical remanence in Tethys sediments (e.g., Crouzet et al. 2003; Schill et al. 2004) (see also Fig. 5). With some exceptions, joint contribution of magnetite and maghemite to the saturation IRM (SIRM) acquired at 3T (maximum available field in this study) reaches up to 80%, with the remaining 20% residing in pyrrhotite and goethite. The magnetic minerals, present in the Triassic carbonates are known to possess largely varying room temperature saturation magnetizations (magnetite: 480 kA/m; maghemite: 380 kA/m; pyrrhotite: 80 kA/m; goethite: 2 kA/m (Dunlop and Özdemir 1997), which in turn are complexly related to SIRM (a grain-size dependent parameter). The magnetic remanence may be overwhelmed even by very small quantities of magnetite and maghemite compared to the other two minerals.

Thermomagnetic curves

Several specimens subjected to acquisition of thermomagnetic (Js-T) curves and their derivatives exhibited variations with characteristics illustrated for two specimens (Fig. 4). Js at the end of the heating-cooling cycle was commonly higher (up to 3.3 times for TMG section) than that at the beginning but nearly the same or even lower values (for TNT section) were found. All curves exhibit maximum negative gradients within the range of 460-520°C. The prominent minimum at 60-80°C during heating may be related to goethite with the Neel temperature of 70-125°C (O'Reilly 1984). Because of weak magnetization, presence of several magnetic carriers in different proportions, thermal alterations leading to formation of new magnetic mineral etc., accurate determination of Curie/Neel temperatures is not easy. In favorable circumstances, however, the Curie temperature of a mineral phase can be precisely determined using the second derivate, as shown by the inset in Fig. 4(a). The peak at 530°C, corresponding to the maximum curvature of the cooling curve (within the range of 400-620°C), is inferred to represent an impure magnetite (e.g., Ti-poor). The position of the cooling curve, for specimen TNT7-2, passing much higher the heating curve implies that much of this magnetite is a product of laboratory heating. Sudden peak (with zero gradient) at ca. 420°C corresponding to a hump during heating but none in the cooling curve in sample TNTN-2 (Fig. 4b) might indicate the transformation of minor amounts of maghemite to hematite (but not magnetite, as the cooling curve follows almost the same path). The gradual decay of the tail and a V-shaped gradient of the heating curve above ca. 600°C in some specimens was attributed to hematite – newly formed during the heating experiment. Finally, magnetite newly formed by alteration of pyrite, maghemite and other Fe-bearing minerals is responsible for the enhanced magnetization at the end of cooling (e.g., Liu et al. 2005).

Magnetic Remanence

Demagnetization behavior

Magnetic behavior during demagnetization varies at specimen level as shown by vector plots and intensity decay curves (Figs. 5,6). Most specimens exhibit the ubiquitous presence of a magnetic component of soft coercivity (<20 mT AFD) and very low T_{ub} (below 150°C or 180°C ThD), characterized by northerly declinations and moderately downward inclinations in geographic coordinates. Denoted as RF, it represents a viscous magnetic overprinting by the recent or present-day field (pdf: northerly directed with ca. 48° inclination at the

sampling location) and it has no paleomagnetic significance. Several specimens with exceptionally high initial NRM intensities subjected to AFD during pilot study showed RF with harder coercivity, requiring 50 mT or above to demagnetize depending on whether the carrier is maghemite or magnetite. Many specimens from all three sections yielded a second component, unblocked below ca. 330°C during further ThD. This intermediate T_{ub} component residing in pyrrhotite (Curie T of ca. 320°C) is labelled as Py (Fig. 5). Py directions group better before bedding-tilt correction. For many specimens initially treated by AFD up to 80 mT and then by ThD steps, the residual NRM at ca. 350°C was too small compared to the magnitude of any of these two components (Fig. 6, upper). Only in specimens for the TMG section subjected to ThD, a significant portion of NRM intensity persisted above 350°C (Fig. 5, left and Fig. 6, lower) and gradually decayed to the instrument noise level by 575-600°C step showing the presence of a high T_{ub} remanence attributed to magnetite (labelled Mt in vector plots; Fig. 5).

Considering the experience of recovering a primary remanence residing in magnetite from the Triassic sediments in Jomsom area (Klootwijk and Bingham 1980), Dolpo (Crouzet et al. 2003), and Manang (Appel et al. 1991), several other combinations of AFD and ThD were attempted. The typical pilot demagnetization sequence involved steps (i) to (v), as follows: (i) initial NRM measurement, (ii) AFD at 20mT (to demagnetize soft coercivity pdf based on maghemite or magnetite), (iii) ThD at 180°C (to demagnetize high-coercivity but low-unblocking temperature goethite-based pdf), (iv) 200-350°C (to demagnetize pyrrhotite-based ChRM), and (v) AFD at >20 to 80 mT (to demagnetize probable medium-coercivity remanence based on magnetite) or ThD up to 600°C (to

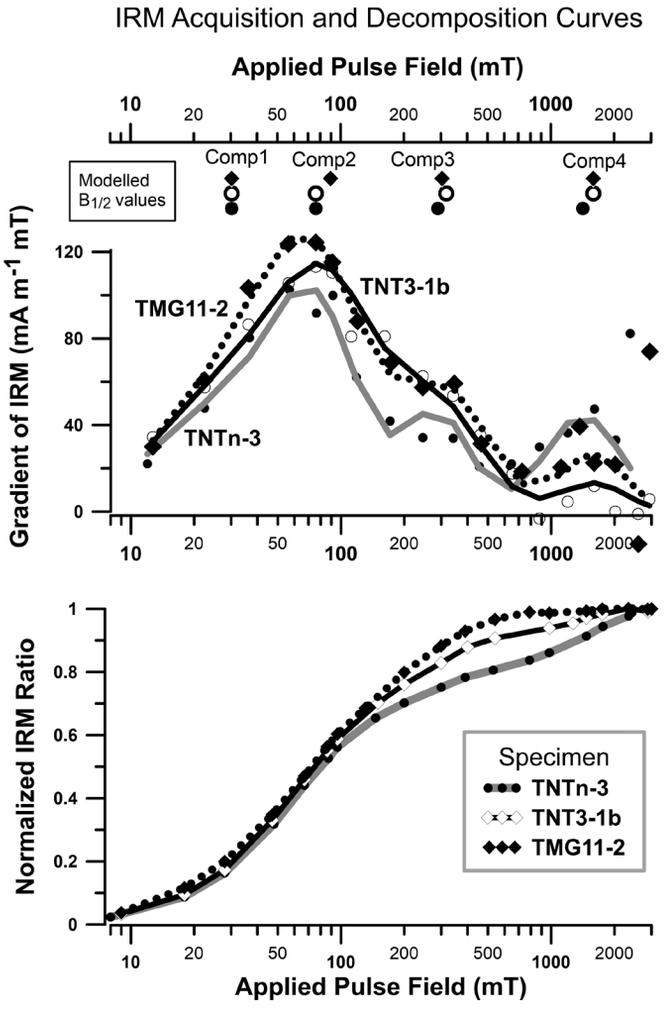

Fig. 3: (a) Results of analysis of the isothermal remanent magnetization (IRM). Lower: Acquired IRM (normalized) curves; Upper: IRM gradient curves, with calculated values (discrete points) and synthetic curves (lines). Each gradient curve is decomposed into 4 components (comp1-comp4) with characteristic parameters (B1/2 and DP) suggested to represent magnetite, maghemite, pyrrhotite, and goethite, respectively. Positions of B1/2 values (mT) are shown along the uppermost axis. Numerical data for each component given in Table 1.

Table 1. Magnetomineralogy based on isothermal remanent magnetization (IRM) data

Specimen	Compo-nent	Contribution to total IRM	$B_{1/2}$	DP	Magnetic mineral inferred
		%	mT	mT	
TNTn-3	Comp1	37.5	30.2	0.35	magnetite
	Comp2	31.7	75.9	0.20	maghemite?
(Upper Mukut Formation, limestone)	Comp3	14.2	288.4	0.15	pyrrhotite
	Comp4	16.7	1412.5	0.18	goethite
TNT3-1b	Comp1	34.0	30.2	0.35	magnetite
	Comp2	40.8	75.9	0.25	maghemite?
(Upper Mukut Formation, black limestone)	Comp3	18.4	316.2	0.20	pyrrhotite
	Comp4	6.8	1584.9	0.15	goethite
TMG11-1b	Comp1	37.9	30.2	0.35	magnetite
	Comp2	41.7	89.1	0.25	maghemite?
(Upper Mukut Formation, limestone)	Comp3	16.7	302.0	0.20	pyrrhotite
	Comp4	3.8	1584.9	0.15	goethite

Note: Component data derived from joint analyses of IRM acquisition and gradient plots following Kruiver et al. (2001). The IRM gradient curve for a specimen can be decomposed into four component curves, each being uniquely defined by the mean remanence coercivity (log ($B_{1/2}$) and the logarithmic dispersion parameter (DP).

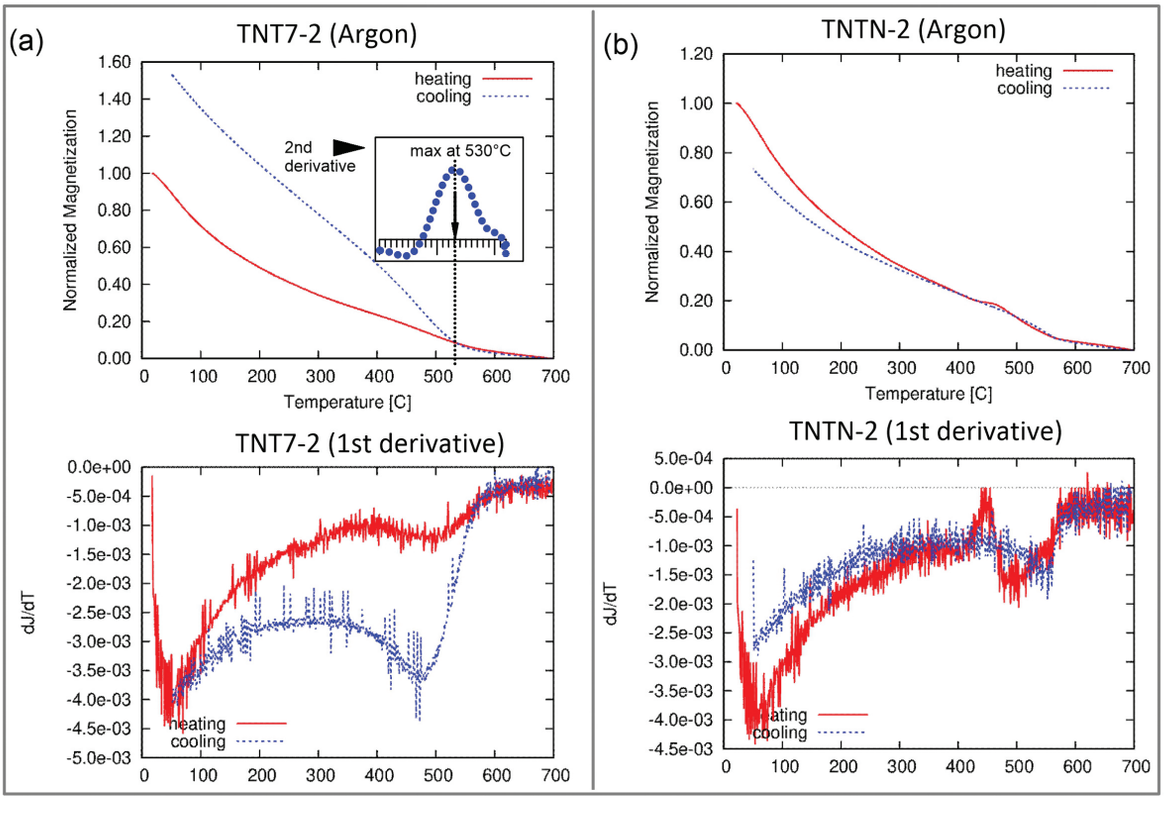

Fig. 4: Thermomagnetic curves (heating and cooling) showing the change in magnetization (upper), their first derivatives (lower) as a function of temperature for representative chip specimens measured using a magnetic balance. Experimental conditions: 500mT applied field, argon atmosphere, and heating-cooling cycle of 25-700°C. These curves indicate the presence of magnetite, maghemite, and goethite, The inset in (a) shows accurate Curie temperature estimation using the second derivative (detailed explanation in the text).

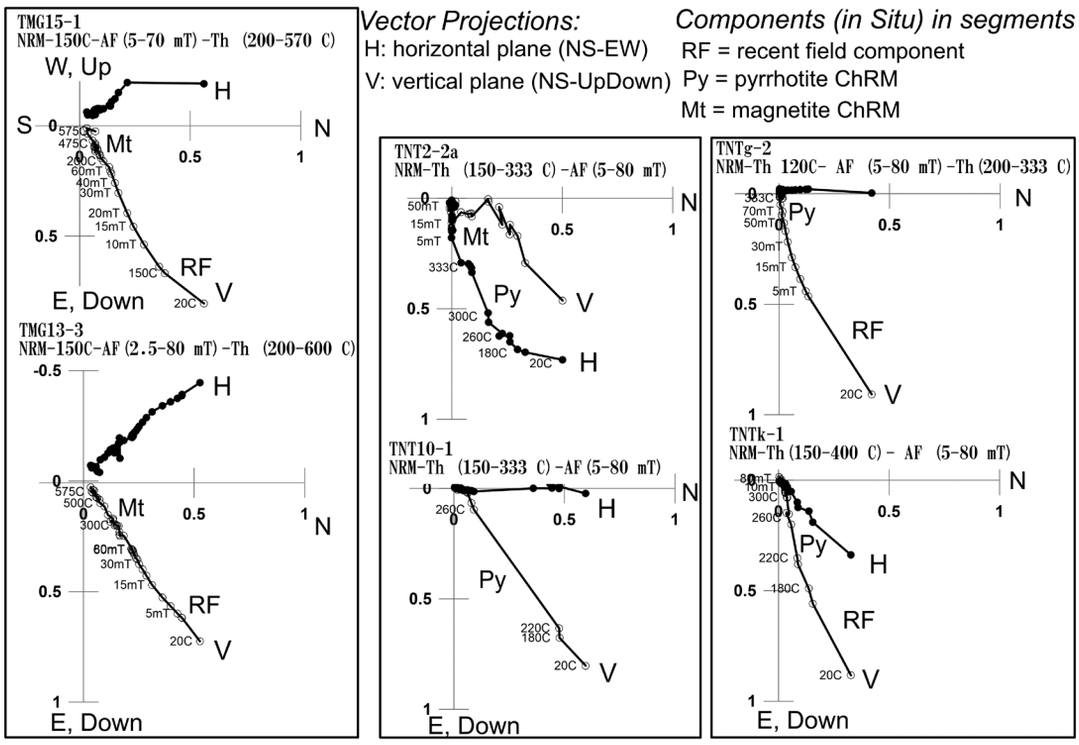

Fig. 5: Zijderveld type vector plots for representative specimens showing their behavior during differing demagnetization sequences involving thermal demagnetization (ThD) and alternating field demagnetization (AFD). Each diagram comprises a pair of projections in NS-EW horizontal plane (filled circle) and NS-UpDown vertical plane (open circle), respectively. The directions are shown in geographic coordinates. Following the NRM (20°C) measurement, almost all specimens were subjected to a ThD step of 150°C to remove the recent field component (RF) for smooth recovery of other components residing on pyrrhotite (Py) and magnetite (Mt) as indicated in vertical projections (V).

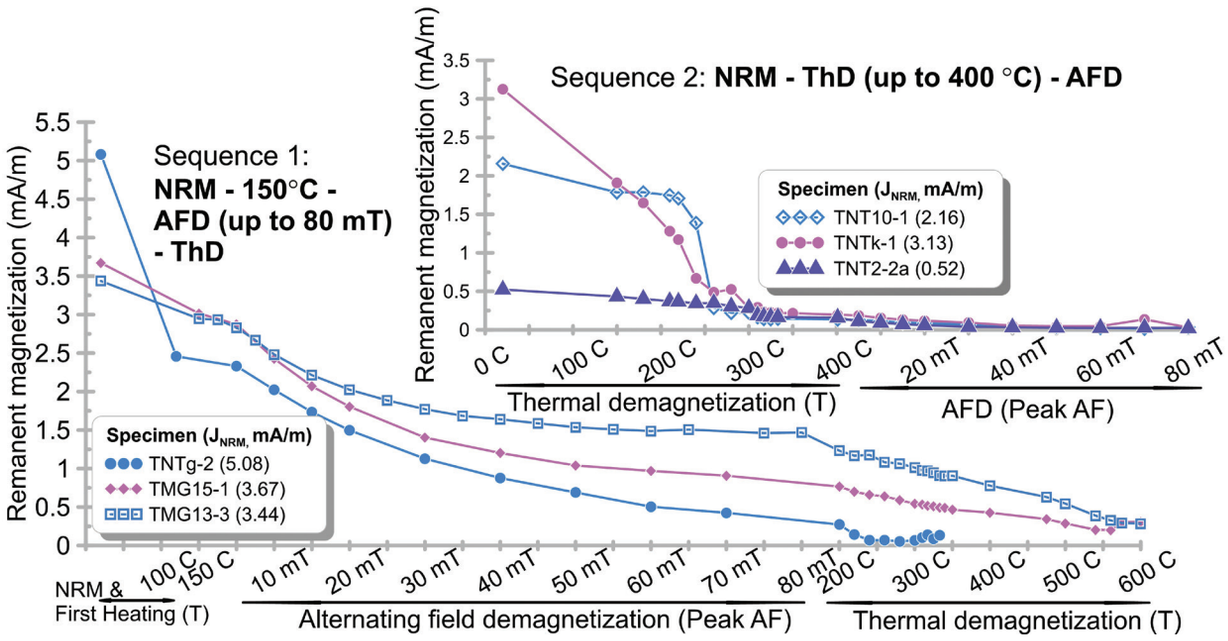

Fig. 6: Intensity decay curves showing varying behavior of specimens, with differing NRM magnitudes, upon demagnetization. Demagnetization sequence 1 is effective in sequentially removing complex remanences residing in goethite, soft magnetite or maghemite, pyrrhotite, and high unblocking temperature magnetite, especially for TMG specimens, as the demagnetization progresses. Sequence 2 is preferred to recover the pyrrhotite-based remanence in TNT specimens lacking in magnetite-based remanence.

demagnetize any remanence carried by magnetite).

Estimation of the characteristic remanences (ChRMpyr and ChRMmag)

Remanence components (RF, Py and Mt) were isolated by joint analysis of NRM intensity decay, stereograms and vector plots, searching for datapoints lying on linear segments or endpoints in the latter. Component RF was ubiquitous, predominant and the only component identified first by its reflection in NRM-150°C step (goethite-based) and/or AFD below 15-20 mT (maghemite-based), but also persisting to demagnetization steps as high as 575-600°C (magnetite-based). Assignment to Py was based on its restricted demagnetization range (mostly 225-350°C) and lack of parallelism with the direction assigned to RF in the same specimen. Component Mt assignment required that the residual intensity after removal of RF and Py is above the noise level and the corresponding line segment above 400°C is not parallel to RF. In a few cases, AFD data were used to determine Mt component using the coercivity ranges of 20-80 mT when well-defined linear segments, with directions different from RF and Py, were present. No clear evidence for the occurrence of antipodal counterparts of any of the components (RF, Py and Mt) were found in the studied specimens. Many TMG specimens with low NRM intensity and predominance of RF or Py over Mt had too low residual intensity even before complete demagnetization of the former (RF or Py) as shown by demagnetization trajectories along great circle (GC). Because of the ambiguity in discriminating the pairs of components describing the GCs, and too short arcs and proximity of their endpoints, reliable estimation of mean directions was impossible. Directional estimates of components (Py and Mt) satisfying the criteria of $\alpha_{95} \leq 15°$ are listed in Tables 2,3. Fisherian mean directions are calculated giving equal weight to specimens due to large scatter of declinations at specimen level. The *in situ* pyrrhotite-based (Py) and magnetite-based (Mt) components, representing well-defined stable remanences, are hereafter designed as characteristic remanences and labelled as ChRMpyr and ChRMmag, respectively. Mean directions and corresponding data are presented in stereograms (Fig. 7) and Table 4.

Interpretation of characteristic remanences

a) Pyrrhotite-based remanence (ChRMpyr)

ChRMpyr directions for three sections in geographic coordinates showing northerly declinations and downward inclinations (56-63°) steeper than the pdf (48°) by 9°-16° (Fig. 7 and Table 4). Due to small variations of bedding attitudes by sampled stratigraphic levels, fold test is not applicable. Considering pyrrhotite as the remanence carrier and inclinations (steeper than RF), ChRMpyr corresponds to similar secondary post-folding remanence recovered from Triassic carbonates of the Tethys Himalaya (e.g., Manang, Shiar and Larkya areas; see Appel et al. 2012). Also, the remanence with intermediate unblocking temperatures (predominantly <270-280°C and occasionally <320°C) included into component A and attributed to viscous magnetization of 'recent field origin' in Thinigaon Limestone (NJUT and NTTR locations) in Klootwijk and Bingham (1980) is believed to correspond to ChRMpyr.

As in other Tethys Himalayan sites to the east and west, ChRMpyr is inferred to be related to tectonic deformation and thermo-tectonic processes. As unblocking temperatures exhibit a wide range (with predominance of 200-300°C; Table 2), the remanence is of single (normal) polarity, and geothermometer-based data indicate relatively low metamorphic temperatures (225-275°C, corresponding to a 'strong diagenetic overprint' as noted in section 2.2 above), the maximum temperatures attained by the host sediments must have remained below the Curie temperature of pyrrhotite (Tc=325°C). Hence, ChRMpyr is likely to be a chemical/ thermochemical remanence (CRM/ (T)CRM) or even a partial thermoremanence ((p)TRM) (Appel et al. 2012). The most likely mechanism is the 'grain growth and cooling' involving the growth of pyrrhotite particles during prolonged heating (several myrs) at elevated temperatures (225-275°C) and acquisition of a CRM after reaching a critical size and/or further acquisition of (T)CRM/(p)TRM upon cooling (Crouzet et al. 2001).

Preservation of ChRMmag together with pyrrhotite in condensed limestones of the TMG section as in Dolpo (Crouzet et al. 2003) further supports the (T)CRM/(p)TRM acquisition by 'grain growth and cooling' mechanism under low maximum metamorphic temperatures (ca. 250°C). Within TNT sections, specific stratigraphic levels characterized by higher degree of magnetic anisotropy and oblate ellipsoids and 'slaty or pencil' cleavage conditions might have experienced somewhat elevated temperatures (Fig. 9 and section 5.2)

Timing of ChRMpyr (with combined Fisherian mean for 3 sites: n=3, D=3.5°, I=58.2°, k=81.4, α_{95}= 13.8°) from Jomsom and linking it to particular deformation phase is not straight forward given the uncertainties in timing of the latest major folding event following which the remanence was acquired, duration of ductile-brittle transition (thermal conditions above ca. 200°C) favoring remanence acquisition, 'grain growth and cooling' mechanism of pyrrhotite acquiring the (T) CRM/(p)TRM, the normal polarity chron during which the remanence acquisition occurred etc. The easiest way is to compare it with the similar normal polarity ChRMpyr (with inclinations steeper than the pdf) recovered from several sampling localities (Hidden Valley, Manang, Nar Phu, Larkya) situated within 28.7-28.8°N latitude, 83.6-84.6°E longitude. In analogy with those mutually close in situ ChRMpyr directions with declinations varying by <20° (353.6 to 16.4°) and inclinations varying by <7° (59.2 to 65.9°), ChRMpyr is assigned a maximum age of ca. 30 Ma (Appel et al. 2012). For comparison with the expected inclination (I_{exp}) at 30 Ma for Jomsom using the Indian Plate apparent polar wander paths, an estimate of 35.0° (after Acton 1999) expected inclination, which is midway of two other estimates (39.8° after Besse and Courtillot (1991) and 29.8° after Vaes et al. (2023)) has been adapted. The observed inclination (I_{obs}) of 58.2° is steeper than Iexp by 23.2±11.6°, which is interpreted as the upper limit of magnitude of inclination steepening of Jomsom area after the acquisition of ChRMpyr. Although observed declinations of *in situ* ChRMpyr at 3 sections deviated by up to ±14°, the observed and expected mean declinations differ by merely 4.0°. When averaged over three sites, therefore, there seems to be no significant rotation of the Jomsom area with respect to the Indian Plate about the vertical.

b) Magnetite-based remanence (ChRMmag)

ChRMmag recovered from the TMG section is similar to the

Table 2: Pyrrhotite-based secondary remanence directions (Tethys Himalaya metasediments, Jomsom)

S. No.	Specimen	Method*	Demagnetization type**	Demagnetization range: mT (AFD), deg.C (ThD)	Directions in geographic coordinates*		Directions in stratigraphic coordinates***		α_{95} (°)	Bedding data	
					Dg (°)	Ig (°)	Ds (°)	Is (°)		Dip dir (°)	Dip angle (°)
TNT1 Section											
1	TNTA-2	LA	AFD	60-80	21.4	47.7	359.7	-69.3	3.6	42	124
2	TNTB-1	LF	Mixed	70-240	355.6	69.8	15.1	-22.2	4.3	26	95
3	TNTB-2A	LF	ThD	240-317	7.0	75.5	21.1	-18.7	2.5	26	95
4	TNTE-1B	LA	AFD	30-60	18.5	46.9	9.2	-65.6	7.5	32	115
5	TNTE-2A	LF	Mixed	50-220	58.5	42.1	77.4	-62.3	2.5	32	115
6	TNTG-1	LF	ThD	180-300	3.7	65.3	38.1	-20.9	0.6	60	98
7	TNTG-2	LA	ThD	60-220	302.3	74.6	46.4	-0.7	8.7	60	98
8	TNTH-1	LF	ThD	180-300	39.0	61.3	40.2	-56.1	1.7	48	118
9	TNTHD-2	LA	Mixed	40-240	7.7	56.0	8.6	-45.9	5.4	12	102
10	TNTI-1	LF	Mixed	70-240	324.0	57.0	346.5	-29.3	6.5	16	101
11	TNTI-2	LF	ThD	280-350	329.8	52.4	343.8	-34.4	2.2	16	101
12	TNTJ-2	LF	ThD	180-350	10.6	72.8	10.3	-47.2	4.3	10	120
13	TNTL-2	LF	ThD	240-325	25.9	53.6	339.7	-77.1	5.2	46	140
14	TNTM-1	LF	Mixed	40-260	359.2	55.1	357.6	-72.9	12.7	1	128
15	TNTM-2	LA	ThD	150-300	9.1	42.5	52.4	-82.4	1.6	1	128
16	TNTN-1	LF	ThD	180-300	2.4	65.7	1.8	-46.3	0.9	1	112
17	TNTN-2	LA	Mixed	80-240	59.3	31.8	67.0	-37.7	8.7	1	112
TNT2 Section											
1	TNT1-1A	LF	ThD	200-280	19.0	50.6	15.8	-11.0	11.8	10	62
2	TNT3-1Ar	LF	ThD	180-325	4.9	60.3	3.1	-22.6	5.6	1	83
3	TNT4-1A	LA	AFD	20-60	37.3	61.1	20.0	-40.9	2.3	354	112
4	TNT5-1A	LF	ThD	200-325	358.4	50.3	1.4	-67.5	3.7	354	118
5	TNT5-2B	LF	ThD	180-300	359.2	56.6	360.0	-61.1	0.7	354	118
6	TNT6-1B	LF	ThD	150-220	50.3	46.4	69.2	-55.7	11.6	1	134
7	TNT7-1	LF	AFD	20-80	18.7	68.2	18.5	-68.0	9.4	1	138
8	TNT8-1A	LF	ThD	220-325	6.0	47.8	54.0	-61.0	1.3	320	150
9	TNT9-1A	LA	ThD	180-300	346.4	52.3	314.1	-68.3	1.2	20	138
TMG Section											
1	TMG1-1B	LF	ThD	250-350	59.1	66.2	35.7	-60.7	12.4	342	156
2	TMG1-2A	LA	ThD	200-280	20.1	57.4	79.6	-70.4	3.3	342	156
3	TMG2-1A	LF	ThD	180-350	20.2	72.0	27.6	-80.5	4.9	12	153
4	TMG2-2	LA	ThD	200-350	19.8	63.7	87.8	-86.5	3.3	12	153
5	TMG3-2B	LF	ThD	180-325	358.7	45.0	235.0	-76.2	2.9	12	146
6	TMG4-1A	LF	ThD	200-240	335.2	52.4	271.9	-65.7	7	16	156
7	TMG4-2A	LF	ThD	250-325	0.3	55.6	239.3	-77.1	1.8	16	156
8	TMG5-2B	LF	ThD	180-325	256.7	48.9	247.2	-50.6	8.7	330	160
9	TMG6-1	LF	ThD	180-260	353.6	51.2	251.8	-67.1	8.8	22	160
10	TMG7-3	LA	ThD	200-240	351.7	42.6	247.4	-58.6	3.4	22	160
11	TMG8-1	LA	Mixed	40-220	328.8	59.2	311.2	-70.6	3.7	356	138
12	TMG8-2B	LF	ThD	180-325	355.4	48.1	286.4	-89.6	3	356	138
13	TMG9-1	LA	ThD	200-240	23.2	41.8	216.8	-65.7	4.9	28	156
14	TMG9-2	LA	ThD	275-350	325.0	53.7	265.0	-72.6	3.6	28	156
15	TMG10-1	LF	ThD	225-325	343.3	53.0	289.1	-64.6	2.6	28	156
16	TMG10-2A	LA	ThD	200-240	332.9	64.5	319.9	-67.6	7.6	28	156
17	TMG11-1B	LF	ThD	225-325	358.5	56.8	331.8	-75.3	1.6	18	138
18	TMG11-2	LF	ThD	200-240	330.6	49.3	308.6	-59.2	9.7	18	138
19	TMG12D-2	LF	ThD	180-275	87.9	56.1	69.7	-48.2	2.5	18	138
20	TMG14-1	LA	ThD	200-310	302.9	50.0	292.4	-55.1	12.4	355	135
21	TMG15-1	LA	ThD	200-340	319.7	48.3	285.6	-65.7	3.6	355	135
22	TMG16-2	LA	ThD	200-300	346.9	56.3	183.8	-76.1	4.1	352	160
23	TMG17-2	LF	ThD	200-325	13.2	48.9	208.6	-58.8	2.4	20	170

* Calculation of remanence directions: PCA (LF = Line Fit; LA = Line Fit with anchor to origin using Palmag 2.0 (Munich)

** ThD: Thermal demagnetization; AFD: Alternating Field demagnetization.

*** Dg, Ig and Ds, Is are the declination and incliantion pairs of characteristic remanence before and after correction for bedding-tilt..

α95 is the error parameter associated with the direction calculated by line-fitting

Table 3: Magnetite-based characteristic remanence directions (Tethys Himalaya metasediments, Jomsom)

S. No.	Specimen	Method*	Demagnetization range**	Geographic coordinates		Stratigraphic coordinates		α_{95}	Bedding data	
				Dg (°)	Ig (°)	Ds (°)	Is (°)	(°)	Dip dir (°)	Dip angle (°)
TMG section										
1	TMG3-2B	LA	350-400°C->5-40 mT	297.8	62.3	323.1	-53.6	3.9	12	146
2	TMG4-2A	LA	5-50 mT (after 400°C)	300.1	54.3	305.5	-53.1	2.2	16	156
3	TMG12-1	LA	360-400°C--> 5-60 mT	311.6	48.0	313.9	-47.0	1.6	18	138
4	TMG12D-2	LA	360°C -> 5-40 mT	312.3	55.6	324.4	-50.3	1.2	18	138
5	TMG13-3	LA	340-560°C	310.4	41.3	306.2	-43.0	3.1	18	138
6	TMG14-1	LF	20-80 mT	312.1	63.8	355.0	-59.7	3.0	355	135
7	TMG15-1	LA	350-540°C	319.4	43.1	273.5	-64.5	4.5	355	135
8	TMG17-1A	LF	30-70 mT	284.0	57.7	310.8	-55.3	2.9	20	170

* Calculation of remanence directions: PCA (LF = Line Fit; LA = Line Fit with anchor to origin using Palmag 2.0 (Munich)

** All specimens subjected to initial ThD step of 150 deg. C

Dg, Ig and Ds, Is are the declination and incliantion pairs of characteristic remanence before and after correction for bedding-tilt..

α_{95} is the error parameter associated with the direction calculated by line-fitting

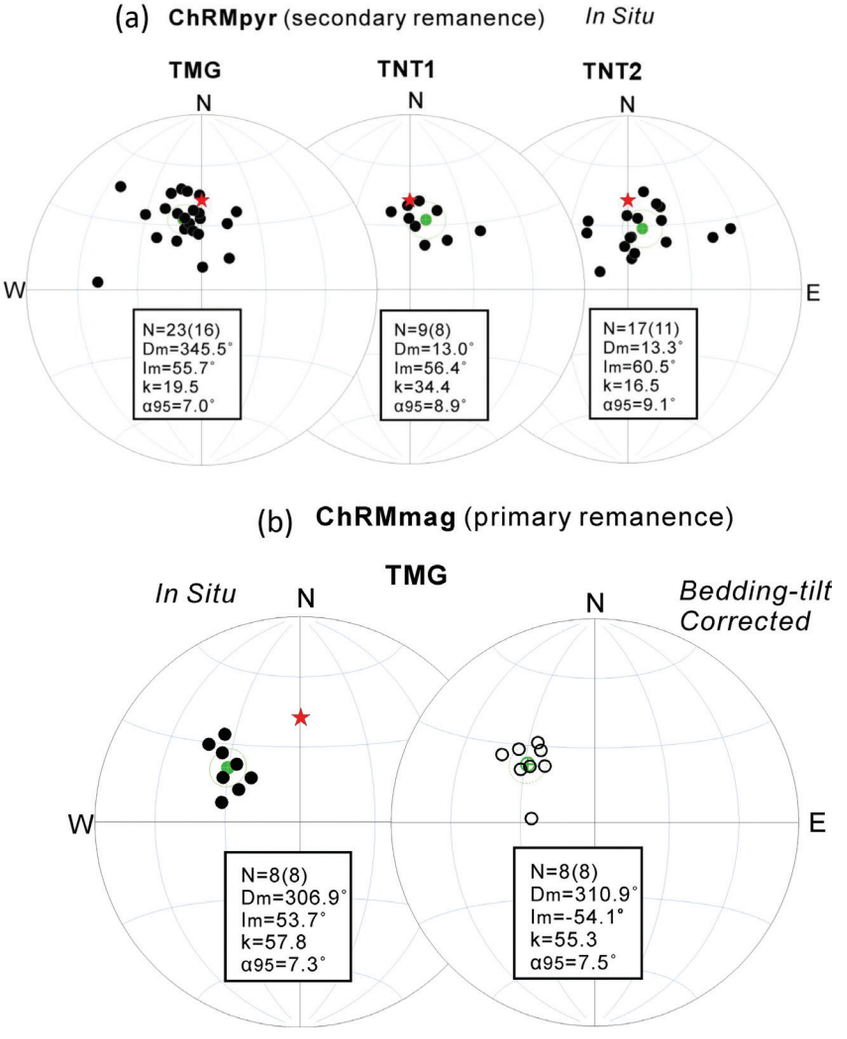

Fig. 7 (a) Summary of in situ characteristic remanence residing in pyrrhotite (ChRMpyr). N is the number of specimens used to calculate the mean directions. Fisherian mean estimates (dots) are provided with the circle of confidence at 95% level, for each section. The present-day field (pdf, with an inclination of 48°) is shown by a star.

(b) Summary of the characteristic remanence residing in magnetite (ChRMmag) recovered from the TMG section. Due to similar bedding attitudes among the sampled levels, fold test is indecisive. In Situ declination of mean ChRMmag in this section is deviated towards west by 39-53° with respect to pdf and ChRMpyr shown in (a).

Table 4: Mean magnetic remanence directions (Tethys Himalaya carbonates, Jomsom)

S. No.	Section	N(n)	Source	Geographic coordinates				Stratigraphic coordinates				Remarks
				Dg (°)	Ig (°)	kg	α_{95}	Ds (°)	Is (°)	ks	α_{95}	
Pyrrhotite-based (CHRMpyr)												
1	TMG	23(16)	This study	345.5	55.7	19.5	7.0					secondary
2	TNT1	9(8)	This study	13.0	56.4	34.4	8.9					secondary
3	TNT2	17(11)	This study	13.3	60.5	16.5	9.1					secondary
	Combined Mean: Number of sections = 3			3.5	58.2	81.4	13.8					
Magnetite-based (CHRMmag)												
1	TMG	8(8)	This study	306.9	53.7	57.8	7.3	310.9	-54.1	55.3	7.5	primary, Triassic
2	KandB11 (NJUT)	22(n.a.)	KandB(1980)	340.0	26.0	n.a.	n.a.	324.5	-43.0	10.0	10.0	primary, Triassic
3	KandB12 (NTTR)	35(n.a.)	KandB(1980)	340.0	9.4	n.a.	n.a.	329.0	-47.0	21.0	5.5	primary, Triassic
	Combined Mean: Number of sections = 3			332.3	30.4	9.3	42.9	322.1	-48.3	96.2	12.6	large improve-ment after unfolding
				ka/kg = 10.3								

KandB(1980) = Klootwijk and Bingham (1980); N(n)=Number of specimens (sampling levels)
Precision k is given after (ka) and before (kb) correction for bedding-tilt

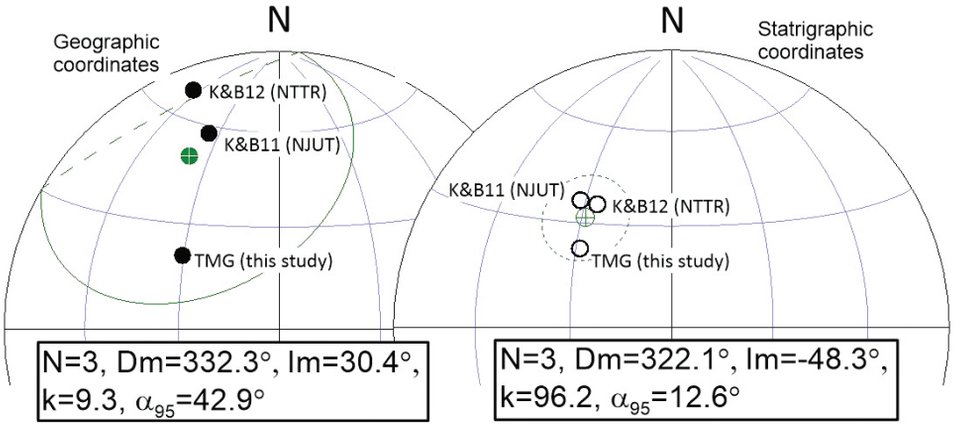

Fig. 8: Comparison of magnetite-based characteristic remanence from three carbonate sections (two sections (KandB11 and KandB12) from Klootwijk and Bingham (1980) and one section (TMG) from this study). Note the drastic improvement in grouping in directions after bedding-tilt correction (k: increase from 9 to 96, and α95: decrease from 43° to 13°) in favor of the acquisition of remanence prior to folding and therefore a primary origin.

Component C (with unblocking temperatures of 300-500°C) of Klootwijk and Bingham (1980). Bedding-tilt correction of ChRMmag results in a mean direction with steep mean inclination (-54.1°). Applying paleomagnetic fold and reversal tests for ChRMmag within the TMG section was not possible because of identical bedding attitudes and single polarity (i.e., normal). But, Combining ChRMmag from TMG section with the mean Component C directions for two sections of Klootwijk and Bingham (1980) leads to a remarkable improvement in grouping around the mean (a ten-fold increase in k and drastic improvement in $\alpha_{95;}$ see Table 4 and Fig. 8). This case is taken as a positive fold test supporting the interpretation of the primary nature of the ChRMmag and C component. The combined mean (n = 3 sections, D=322.1°, I=-48.3°, k=96.2, α_{95}= 12.6°) is suggested to be representative of the Triassic Carbonates from Jomsom.

Considered together, the mean directions at three sections (corresponding to Induan to Norian stages with inferred duration of 251.9-208.5 Ma) have declination range of 311° to 329° and inclination range of -54° to -43°. In the meantime, the expected remanent magnetization directions at Jomsom for the same duration from the Indian Plate global apparent polar wander paths data are seen as follows: (i) D_{exp}: 315° to 327°, I_{exp}: -59° to -39°after Torsvik et al. (2008); and (ii) D_{exp}: 316° to 307°, I_{exp}: -53° to -43° after Vaes et al. (2023). From comparison of the ranges of observed and expected ranges for D and I, ChRMmag directions are inferred as primary remanence acquired by these Triassic rocks during deposition in the southern hemisphere at paleolatitudes of about 34.5°S to 25°S.

MAGNETIC FABRIC BASED ON ANISOTROPY OF MAGNETIC SUSCEPTIBILITY (AMS)

The magnetic susceptibility (k) is a physical property of a

material that indicates its capacity to acquire magnetization (J) under an applied magnetic field (H) following the relationship $\mathbf{J}j = k_{ij}\mathbf{H}_j$ (i,j = 1,2,3), where both J and H are vector quantities. At low applied fields, the magnetization is linear, and the susceptibility is field independent. The lattice alignment of crystals with magnetocrystalline anisotropy and/or shape alignment of ferromagnetic grains in a rock contribute to the anisotropy of magnetic susceptibility (AMS). The rock fabric that commonly involves the preferential distribution-orientation of the constituting minerals gives rise to magnetic anisotropy. For an anisotropic rock specimen, the susceptibility k varying with the direction of measurement is a 3×3 symmetric second-rank tensor. In general, there exists a Cartesian coordinate system in which the nondiagonal components of the susceptibility tensor are zero and such tensor represents a triaxial susceptibility ellipsoid, defined by three principal susceptibilities ($k_1>k_2>k_3$) with corresponding maximum (k_{max}), intermediate (k_{int}) and minimum (k_{min}) directions. Thus, the AMS ellipsoid reflects the magnetic (susceptibility and its anisotropy) and dimensional (shape, size, and preferential orientation) properties of constituents integrated over a volume of rock. The magnitude of bulk susceptibility of a rock largely determined by the relative content of a few magnetically important ferromagnetic minerals, but in the Triassic carbonates other minerals such as the diamagnetic calcite is important. Ferromagnetic minerals (typical susceptibility magnitudes) relevant to carbonates are: magnetite ($0.2\text{-}1.2\times10^{-3}$ m^3kg^{-1}), maghemite ($0.3\text{-}0.5\times10^{-3}$ m^3kg^{-1}), pyrrhotite ($0.07\text{-}0.01\times10^{-3}$ m^3kg^{-1}, and goethite ($0.0005\text{-}0.0015\times10^{-3}$ m^3kg^{-1}) (Lascu et al. 2010 and references therein). Other types of weakly magnetic minerals, namely, diamagnetic (calcite: -8×10^{-9} m^3kg^{-1}, water and organic matter: -9.0×10^{-9} m^3kg^{-1}, quartz: -6.0×10^{-9} m^3kg^{-1}), paramagnetic and imperfect antiferromagnetic minerals ($0.1\text{-}7\times10^{-6}$ m^3kg^{-1}) (Rochette, 1987; Lascu et al., 2010) may be the significant susceptibility contributors especially in the weak sedimentary rocks.

Basic AMS parameters

In this study, the magnetic fabric in a rock sample is characterized by (i) three principal AMS magnitudes and directions (maximum k_{max} ≥ intermediate k_{int} ≥ minimum k_{min}), (ii) shape or quality parameter (T), and (iii) quantity expressed as the corrected degree of anisotropy (P_J). T and P_J are calculated as follows (Jelinek 1981):

$$T = \left(2\eta_{\text{int}} - \eta_{\max} - \eta_{\min}\right)/\left(\eta_{\max} - \eta_{\min}\right)$$

$$P_J = \exp\sqrt{2\left[\left(\eta_{\max} - \eta_m\right)^2 + \left(\eta_{\text{int}} - \eta_m\right)^2 + \left(\eta_{\min} - \eta_m\right)^2\right]}$$

where, $\eta_{max} = \ln k_{max}$; $\eta_{int} = \ln k_{int}$; $\eta_{min} = \ln k_{min}$; $\eta_m = \ln k_m$, and

$k_m = (k_{max} + k_{int} + k_{min})/3$ is the mean magnetic susceptibility.

Distribution patterns of the principal directions (k_{max}, k_{int}, k_{min}) and ranges of T determine the linear or planar nature of the magnetic fabric. At the scale of sampling level, site or section, clustered k_{min} axes correspond to the pole of the "magnetic foliation plane", whereas clustering of the k_{max} axes defines the "magnetic lineation". Ranges of the anisotropy shape parameter $0<T\leq 1$ and $-1\leq T< 0$ point to oblate (planar) and prolate (linear) fabrics, respectively.

Magnetic fabric may be a composite of AMS patterns, which reflect contributions from multiple ferromagnetic (sensu lato), paramagnetic, and diamagnetic minerals that grew, transformed and mobilized at different times and mechanisms associated with depositional, diagenetic, and tectonic processes (Weil and Yonkee 2009). Calcite in carbonates may be a strain-sensitive petrofabric indicator due to preferred crystallographic orientation of its c-axes due to crystal-plastic deformation mechanisms. Such crystallographic orientation may result in alignment parallel to the direction of maximum shortening (Calvin et al. 2018).

Magnetic susceptibility and magnetic fabric in carbonates from Jomsom

Magnetic fabric parameters, both scalar and directions at specimen level from Jomsom are presented in Table 5. The scalar parameters are illustrated in Fig. 9. Except for a few TMG specimens, k_m is lower than 20×10^{-8} m^3kg^{-1} (i.e., about 500 μSI, assuming an average density of 2500 kg/m^3) implying to the predominance by paramagnetic contribution, while the maximum P_J is 1.12. Samples with low anisotropy degree (P_J<1.02 or 1.03) show no correlation of k_m with P_J or T. Magnetic fabric seems to be complex, and its meaningful interpretation requires breakdown of the datasets by magnitudes of P_J and k_m by setting numerical bounds. Figure 9 reveals the following peculiarities: (i) A strong and positive linear relationship between k_m and T when P_J exceeds a threshold level of ca. 1.03, and a tendency for T to shift from prolate through neutral to oblate region as P_J increases; and (ii) A predominantly prolate fabric below certain threshold of P_J < 1.03.

Diamagnetic minerals must have diluted the susceptibility magnitudes, but clear negative correlation between k_m and P_J lends no support to significant diamagnetic contribution. Most specimens exhibit AMS magnitudes consistent with predominance by paramagnetic minerals such as magnetocrystalline phyllosilicates. Occasionally clear positive correlation between P_J and k_m, however, points to the influence of ferromagnetic minerals (e.g., magnetite, pyrrhotite, goethite).

Mean susceptibility (k_m) and anisotropy degree (P_J) within the lower half of the TNT1 section (with uniform calcareous lithologies) increase gradually (km exponentially, PJ linearly) with depth (Fig. 9, shaded parts in the middle). With some exceptions, the fabric shape (T) too changes within the section from almost neutral (above 10m) to oblate (below 10 m) within this section (Fig. 2, middle). The NRM moment contributed by remanence-carrying minerals, however, had random oscillations. Positive correlations between specific ranges of k_m and T versus P_J occur in all three sections (Fig. 9, shaded parts). Such trends reflect the increasing degree of deformation with depth. This case resembles to that of the development of 'slaty cleavage' (e.g., the pencil cleavage developed within Knob Formation but still far from the 'shear zone' in mudrocks) suggested by Pares et al. (2004).

AMS directions, magnetic fabric patterns, and their relationship to the deformation phases

Principal AMS directions (k_{max}, k_{int}, k_{min}) of specimens from each section, with measured bedding planes (great circles), are shown in Fig. 10a-c using data already presented in Table 5. Each section exhibits an *in situ* composite fabric comprising 2

or 3 directional groupings of k_{max} axes. While about two thirds of the k_{max} and k_{int} axes (defining magnetic foliation) show proximity to the bedding plane traces in these sections, there are differences in k_{min} axes among sections, from random to girdle distribution in great circle trajectories. Below, the prominent patterns (Fig. 10d-g) will be suggested by adapting objective criteria based on the bounds of AMS parameters and seeking their links with structural elements linked to deformation phases. Also, the degree of clustering of ellipsoids before and after bedding correction will be used to interpret the patterns.

Magnetic Fabric Pattern 1

Bulk susceptibility magnitude (k_m) exceeds $20\times10^{-8}m^3kg^{-1}$ (500 μSI) only in specimens from TMG section (Fig. 9, left) being restricted to brachiopod-bearing limestones. In the plot of principal AMS axes in these specimens (Fig. 10d), no parallelism is observed between bedding and magnetic foliation in geographic coordinates. Bedding-tilt corrected data reveal sub-vertical mean magnetic lineation (331.1°/75.5°) and subhorizontal ENE-WSW trending minimum axes (mean: 72.7°/3.0°). AMS scalar parameters (Fig. 9, left) show widely varying from moderately prolate to moderately oblate (T: -0.72 to +0.7) and very low (<1.024) overall anisotropy degree. This magnetic fabric is categorized as pattern 1 (MFP1). Visual inspection of the principal AMS axes for a majority of the remaining TMG specimens (with $k_m < 20\times10^{-8}$ m^3kg^{-1} and P_J <1.04 (excluding a few outliers such as ammonitico rosso), or isolation of dataset restricted to reasonably vertical (i.e., dips > 60°, after bedding-tilt correction) k_{min} axes, reveals parallelism between magnetic foliation and bedding plane in about 40% of the specimens. The k_{max} axes show either E-S or N-W trends. A composite fabric in which the relict primary sedimentary-compactional fabric coexists with an initial tectonic fabric (e.g., due to incipient layer parallel shortening) is inferred. Further elaboration is difficult due to the lack of objective criteria to separate the data subsets.

Magnetic Fabric Pattern 2

For the TNT section, AMS axes for specimens with P_J exceeding 1.04 are shown in geographic coordinates in Fig. 10e,f. The magnetic fabric, visually similar in both sections, comprises magnetic foliations subparallel to bedding and magnetic lineations (sub-horizontal and WNW-ESE directed). For section TNT2, the range of T is between -0.38 to 0.33 (i.e., ellipsoids change from weakly prolate to moderately oblate, almost linearly with increase in anisotropy degree (Fig. 9, right)). Almost identical P_J-T behavior is obvious also for site TNT1 section (Fig. 9, middle). This magnetic fabric is recognized as pattern 2 (MFP2), for which magnetic lineations (with average trends shown by arrows) are subparallel to the fold axes or bedding strikes. Bedding-tilt correction (not shown) leads to shift of k_{min} axes to subvertical positions in both sections, but the k_{max} axes tend to disperse (despite maintaining an average E-W trend). These observations suggest MFP2 to

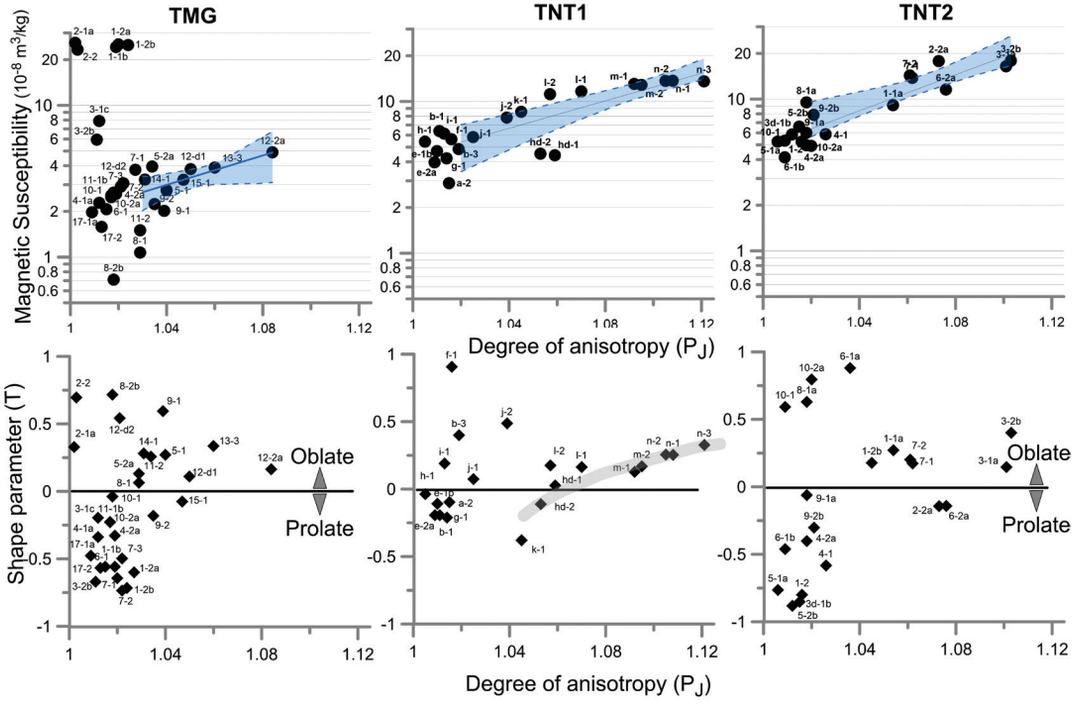

Fig. 9: Scalar AMS parameters for three sections studied. The diagrams are arranged in such a way that the variation of the mean susceptibility magnitude (upper) and shape parameter (lower) with increasing degree of anisotropy (P_J) can be readily seen. Note the exponential increase in mass-specific susceptibility with anisotropy degree when the latter exceeds 1.03-1.04. In several specimens (see the upper left corner), the mean susceptibility exceeds 20 $\times10^{-8}$ m^3kg^{-1} (ca. 500 μSI) implying that paramagnetic minerals no more predominate it. Ranges of logarithmic susceptibility or shape parameter versus degree of anisotropy with notable positive correlation are shown by shades and or line fits with error limits of one standard deviation. For data, refer to Table 5.

Table 5: Magnetic fabric parameters at specimen level from Jomsom

S. No.	Specimen*	Lithology**	Bedding data		AMS parameters**							Geographic coordinates***				Stratigraphic coordinates***			
			Dip dir	Dip angle	MS (10^{-8} m^3kg^{-1})	L	F	P	P_J	T	U	Ig max	Dg max	Ig min	Dg min	Is max	Dsmax	Is min	Ds min
TNT1 Section																			
1	TNTa-2	lmst, black	42	124	2.89	1.008	1.007	1.015	1.015	-0.097	-0.100	6.4	121.0	6.8	30.5	12.6	312.8	60.7	66.0
2	TNTb-1	lmst, black	26	95	6.38	1.007	1.004	1.011	1.011	-0.194	-0.200	17.7	219.8	47.2	109.6	63.5	355.4	8.0	249.0
3	TNTb-3	lmst, black	26	95	4.86	1.006	1.013	1.019	1.019	0.399	0.400	0.2	52.4	20.3	141.8	63.2	305.5	22.1	91.7
4	TNTe-1b	lmst, black	32	115	4.71	1.005	1.004	1.010	1.010	-0.109	-0.100	73.8	189.6	15.8	19.6	9.9	218.2	75.2	85.9
5	TNTe-2a	lmst, black	32	115	3.97	1.005	1.003	1.009	1.009	-0.193	-0.200	49.2	108.4	22.5	324.4	27.3	257.7	28.8	135.1
6	TNTf-1	lmst, black	55	98	5.64	1.001	1.014	1.014	1.016	0.907	0.900	44.3	196.4	23.0	312.1	27.2	85.1	8.6	349.8
7	TNTg-1	lmst, black	60	98	4.22	1.008	1.005	1.013	1.014	-0.211	-0.200	11.5	105.3	58.7	355.3	45.2	321.7	19.8	210.0
8	TNTh-1	lmst, black	48	118	5.44	1.002	1.002	1.005	1.005	-0.038	0.000	16.3	310.6	6.6	42.7	1.3	155.8	68.0	62.1
9	TNThd-1	lmst, black	12	102	4.42	1.028	1.030	1.059	1.059	0.027	0.000	26.2	281.9	35.7	32.8	5.2	127.7	59.7	226.9
10	TNThd-2	lmst, black	12	102	4.52	1.029	1.023	1.053	1.053	-0.112	-0.100	28.7	279.4	26.7	26.3	3.5	130.7	70.1	232.2
11	TNTi-1	lmst, black	16	101	6.14	1.005	1.008	1.013	1.013	0.190	0.200	21.1	298.3	60.3	71.1	15.3	125.1	26.4	223.0
12	TNTj-1	lmst, black	10	120	5.82	1.011	1.013	1.025	1.025	0.074	0.100	40.0	356.3	48.4	158.3	75.0	145.5	6.6	30.6
13	TNTj-2	lmst, black	10	120	7.83	1.009	1.028	1.037	1.039	0.487	0.500	40.6	331.0	49.1	156.5	56.8	129.3	5.4	31.3
14	TNTk-1	lmst, black	35	120	8.56	1.030	1.014	1.044	1.045	-0.379	-0.400	18.5	322.0	51.2	207.3	23.5	133.5	8.5	39.8
15	TNTl-1	lmst, black	46	140	11.66	1.029	1.040	1.070	1.070	0.164	0.100	17.7	291.6	63.7	60.7	1.2	345.8	74.2	250.4
16	TNTl-2	lmst, black	46	140	11.16	1.023	1.033	1.057	1.057	0.175	0.200	23.1	285.4	51.1	46.1	0.0	353.6	88.9	228.3
17	TNTm-1	shale	1	128	13.06	1.039	1.051	1.092	1.092	0.128	0.100	12.6	95.3	41.7	353.5	4.4	258.5	83.2	126.6
18	TNTm-2	shale	1	128	12.87	1.038	1.054	1.095	1.095	0.170	0.100	9.8	93.1	38.7	354.6	4.4	262.0	84.9	101.4
19	TNTn-1	shale	1	112	13.69	1.038	1.066	1.107	1.108	0.254	0.200	12.9	96.8	47.9	353.4	0.5	76.9	63.4	169.6
20	TNTn-2	shale	1	112	13.64	1.037	1.064	1.104	1.105	0.255	0.200	12.7	106.4	44.9	4.1	9.1	73.2	66.9	186.6
21	TNTn-3	shale	1	112	13.59	1.039	1.077	1.119	1.121	0.327	0.300	14.5	102.9	42.6	359.5	5.2	73.0	69.3	178.0
TNT2 Section																			
22	TNT1-1a	ss f, calc	10	62	9.13	1.019	1.034	1.054	1.054	0.272	0.300	14.8	97.4	14.4	193.4	4.7	85.7	76.1	203.9
23	TNT1-2	ss f, calc	10	62	5.24	1.013	1.001	1.015	1.016	-0.800	-0.800	15.5	180.1	72.6	329.4	74.5	151.8	14.3	358.4
24	TNT1-2b	ss f, calc	10	62	8.75	1.018	1.026	1.044	1.045	0.178	0.200	1.3	99.5	5.5	189.5	0.2	98.6	67.5	188.6
25	TNT2-2a	ss f, calc	30	119	17.80	1.041	1.031	1.073	1.073	-0.144	-0.200	12.0	119.3	54.9	11.1	6.3	289.8	60.7	187.7
26	TNT3-1a	ss f, calc~lmst	1	83	16.48	1.042	1.057	1.101	1.101	0.146	0.100	13.7	101.2	5.6	9.2	11.5	78.4	75.0	214.2
27	TNT3-2b	ss f, calc~lmst	1	83	17.93	1.029	1.069	1.101	1.103	0.400	0.400	22.2	102.5	14.8	6.4	13.3	69.8	67.6	194.8
28	TNT3d-1b	lmst, black	8	115	5.85	1.010	1.001	1.011	1.012	-0.882	-0.900	25.5	335.0	8.8	240.6	60.2	106.1	28.6	304.6
29	TNT3d-2	lmst, black	8	115	n.a.	n.a.	n.a.	n.a.	n.a.	n.a.	n.a.	28.5	322.3	51.0	189.2	49.3	113.5	14.0	7.2
30	TNT4-1	ss f, calc~lmst	354	112	5.86	1.019	1.005	1.024	1.026	-0.583	-0.600	21.5	0.1	61.9	220.4	84.3	268.0	1.7	154.1
31	TNT4-2a	ss f, calc~lmst	354	112	4.96	1.012	1.005	1.017	1.018	-0.402	-0.400	19.3	2.2	61.3	230.4	81.9	282.2	4.7	150.4
32	TNT5-1a	lmst, black	354	118	5.24	1.005	1.001	1.006	1.006	-0.765	-0.800	11.4	349.1	10.4	81.6	72.8	10.3	7.0	255.9
33	TNT5-2b	lmst, black	354	118	6.58	1.012	1.001	1.013	1.015	-0.852	-0.900	13.9	348.0	75.2	159.2	74.8	17.0	13.7	177.8
34	TNT6-1a	lmst, black	1	134	7.07	1.002	1.030	1.032	1.036	0.881	0.900	46.9	34.1	43.0	215.0	66.8	252.1	2.2	156.8
35	TNT6-1b	lmst, black	1	134	4.13	1.006	1.002	1.009	1.009	-0.462	-0.500	41.7	115.5	28.8	356.5	13.9	225.4	74.3	15.9
36	TNT6-2a	lmst, black	354	112	11.57	1.042	1.032	1.075	1.076	-0.142	-0.200	20.7	102.0	47.7	348.3	7.8	57.9	63.9	165.2
37	TNT7-1	lmst, black	1	138	13.81	1.025	1.036	1.061	1.062	0.173	0.200	21.0	106.0	50.0	349.9	6.0	246.1	82.5	110.5
38	TNT7-2	lmst, black	1	138	14.33	1.024	1.036	1.061	1.061	0.202	0.200	19.4	108.7	47.0	355.0	3.2	245.2	85.8	79.4
39	TNT8-1a	lmst, black	320	150	9.52	1.003	1.014	1.017	1.018	0.630	0.600	26.1	313.3	46.8	191.8	55.8	330.8	24.8	103.6
40	TNT9-1a	lmst, black	20	138	5.99	1.010	1.009	1.018	1.018	-0.062	-0.100	15.1	107.9	73.3	269.6	12.5	281.3	40.2	179.4
41	TNT9-2b	lmst, black	20	138	7.89	1.014	1.007	1.021	1.021	-0.303	-0.300	2.4	111.6	57.6	206.0	0.7	287.2	15.7	196.7
42	TNT10-1	lmst, black	278	71	5.33	1.002	1.007	1.008	1.009	0.593	0.600	32.0	330.6	38.5	210.8	18.3	143.2	4.8	51.6
43	TNT10-2a	lmst, black	278	71	4.92	1.002	1.017	1.019	1.020	0.796	0.800	64.6	43.4	24.5	207.0	31.9	302.3	8.4	37.6
TMG Section																			
44	TMG1-1b	lmst, brachio	342	156	24.23	1.014	1.004	1.018	1.019	-0.559	-0.600	52.8	350.7	4.9	86.7	76.1	319.6	1.4	56.6
45	TMG1-2b	lmst, brachio	342	156	25.20	1.016	1.003	1.019	1.020	-0.643	-0.600	50.4	338.9	6.1	77.7	74.3	349.3	3.2	244.3
46	TMG1-2a	lmst, brachio	342	153	25.00	1.019	1.003	1.022	1.024	-0.716	-0.700	46.2	351.1	8.5	252.7	72.5	320.7	7.9	75.2
47	TMG2-1a	lmst, brachio	12	153	25.80	1.001	1.001	1.002	1.002	0.328	0.300	67.3	248.6	19.0	103.8	46.6	164.1	16.1	271.5
48	TMG2-2	lmst, brachio	12	146	23.26	1.000	1.002	1.003	1.003	0.695	0.700	44.5	19.0	14.2	275.0	77.7	347.9	7.9	115.7
49	TMG3-1c	lmst	12	146	7.89	1.007	1.005	1.011	1.012	-0.196	-0.200	61.9	345.8	20.7	122.5	75.4	136.7	6.3	253.9
50	TMG3-2b	lmst	12	156	5.93	1.008	1.002	1.010	1.011	-0.670	-0.700	58.6	275.1	29.9	73.4	48.9	140.0	38.6	295.0
51	TMG4-1a	lmst	16	156	2.28	1.008	1.004	1.012	1.012	-0.339	-0.300	6.3	152.2	46.2	248.7	11.1	60.5	29.3	156.9
52	TMG4-2a	lmst	16	160	2.61	1.012	1.006	1.018	1.019	-0.328	-0.300	31.9	3.5	30.8	252.4	51.2	33.0	18.6	147.0
53	TMG5-1	lmst	330	160	2.76	1.014	1.025	1.040	1.040	0.270	0.300	34.6	144.4	54.7	328.2	14.7	154.8	74.7	333.9
54	TMG5-2a	lmst	330	160	3.95	1.012	1.021	1.033	1.034	0.257	0.200	32.9	138.2	54.9	343.6	13.3	160.2	73.7	301.1
55	TMG6-1	lmst	22	160	2.07	1.011	1.003	1.014	1.015	-0.558	-0.600	14.9	113.7	51.4	223.1	13.4	285.3	32.3	186.6
56	TMG7-1	lmst	22	160	3.76	1.020	1.005	1.025	1.027	-0.600	-0.600	27.7	124.4	15.6	223.3	21.8	270.7	3.1	1.5
57	TMG7-2	lmst	22	160	3.06	1.018	1.003	1.021	1.022	-0.735	-0.700	20.7	132.2	44.2	20.7	12.8	266.2	64.2	24.1
58	TMG7-3	lmst	22	160	3.07	1.016	1.005	1.022	1.022	-0.498	-0.500	25.2	126.9	43.9	10.1	18.7	269.4	63.2	41.2
59	TMG8-1	lmst	356	138	1.07	1.013	1.015	1.029	1.029	0.064	0.100	52.7	244.3	17.9	358.8	26.2	137.1	59.8	350.7
60	TMG8-2b	lmst	356	138	0.71	1.002	1.014	1.016	1.018	0.716	0.700	21.7	346.8	63.0	130.6	62.6	14.8	26.7	197.2
61	TMG9-1	lmst	28	156	2.02	1.007	1.029	1.037	1.039	0.594	0.600	2.8	304.2	79.8	47.2	5.1	113.5	75.3	221.3
62	TMG9-2	lmst	28	156	2.24	1.021	1.014	1.035	1.035	-0.181	-0.200	2.1	279.4	55.4	12.7	5.5	315.9	77.1	70.2
63	TMG10-1	lmst	28	156	2.66	1.010	1.009	1.018	1.018	-0.038	0.000	16.5	233.3	51.1	345.1	5.4	3.7	63.9	104.4
64	TMG10-2a	lmst	28	156	2.49	1.011	1.007	1.017	1.017	-0.229	-0.200	18.4	243.1	51.6	358.6	1.5	354.9	69.4	88.1
65	TMG11-2	lmst	18	138	2.55	1.011	1.007	1.017	1.017	-0.227	-0.200	8.7	102.3	75.0	225.0	10.2	286.4	34.3	189.8
66	TMG11-1b	lmst	18	138	1.50	1.013	1.017	1.029	1.029	0.131	0.100	16.4	100.9	25.7	198.4	16.8	281.9	16.3	17.6
67	TMG12-2a	lmst	18	138	2.92	1.005	1.015	1.020	1.021	0.542	0.500	78.7	190.9	9.4	39.4	36.8	199.7	47.4	345.8
68	TMG12-d1	lmst, red (Am R)	18	138	4.90	1.034	1.048	1.084	1.084	0.163	0.100	19.5	208.0	63.3	73.8	21.9	7.8	56.4	240.1
69	TMG12-d2	lmst, red (Am R)	18	138	3.80	1.022	1.027	1.050	1.050	0.110	0.100	26.4	209.4	51.0	80.4	14.9	7.5	50.6	259.4
70	TMG13-3	lmst	18	138	3.89	1.019	1.039	1.059	1.060	0.336	0.300	40.9	110.5	43.5	322.8	27.7	256.5	52.0	122.4
71	TMG14-1	lmst	355	135	3.24	1.011	1.020	1.031	1.031	0.281	0.300	17.9	96.7	53.1	342.0	4.7	244.2	78.3	133.3
72	TMG15-1	lmst	355	135	3.23	1.025	1.021	1.047	1.047	-0.075	-0.100	26.1	108.1	64.1	293.4	3.6	230.8	51.5	136.8
73	TMG17-1a	lmst	20	170	1.97	1.006	1.002	1.008	1.009	-0.477	-0.500	48.5	35.5	41.8	215.5	58.0	0.4	32.1	186.4
74	TMG17-2	lmst	20	170	1.58	1.010	1.003	1.013	1.013	-0.568	-0.600	34.9	51.4	54.6	216.1	43.2	344.1	44.9	186.9

* Data are presented for each specimen level, without averaging at sampling level, owing to significant variations among specimens.

** ss f = sandstone, fine; calc = calcareous; lmst = limestone; brachio = brachiopod-bearing; Am R = Ammonitico Rosso

*** AMS = Anisotropy of Magnetic Susceptibility; L = Magnetic Lineation; F = Magnetic Foliation; P = Degree of Anisotroy; PJ = Jelinek's (corrected) Degree of Anisotropy; T: Shape Parameter

** I and D denote inclination and declination of principal AMS directions (max: maximum, min: minimum) in the coordinates mentioned. Bedding data and remanence directions are expressed in degrees.

be synchronous with folding.

Magnetic fabric pattern 3

Figure 10g shows the principal AMS axes for TNT2 specimens represented exclusively by black limestone and with P_J<1.04. In geographic coordinates, the mean magnetic foliation is NW-SE striking with moderate dip (38°) towards NNE. No parallelism exists between magnetic foliation and bedding. The shape of AMS ellipsoid ranges from weakly prolate to highly oblate (-0.21<T<0.91). This pattern is termed as magnetic fabric pattern 3 (MFP3). Bulk susceptibility magnitude (k_m) is low (4.13-9.52×10^{-8} m^3kg^{-1} with an average of 6.04×10^{-8} m^3kg^{-1}) due to negligible contribution by ferromagnetic minerals.

Godin (2003) recognized several structural domains, with distinct deformation phases and characteristics, in diverse lithologies in the Tethyan domains, of which "domain 5" covers sections in this study. Several MFPs besides a partly preserved initial sedimentary-compactional fabric recognized here point to multiple patterns co-existing in the same section. MFP1 is suspected to be of tectonic origin (e.g., related to preferred orientation of paramagnetic and/or minor amount of ferromagnetic minerals confined to subvertical structure). It may arise from a spaced N-S cleavage formed by E-W extension. Because of the very low anisotropy degree, it is difficult to use a more definitive criterion, such as a positive trend in T-P_J relationship accompanying the development of cleavage, to support this inference. Intuitively, the magnetic

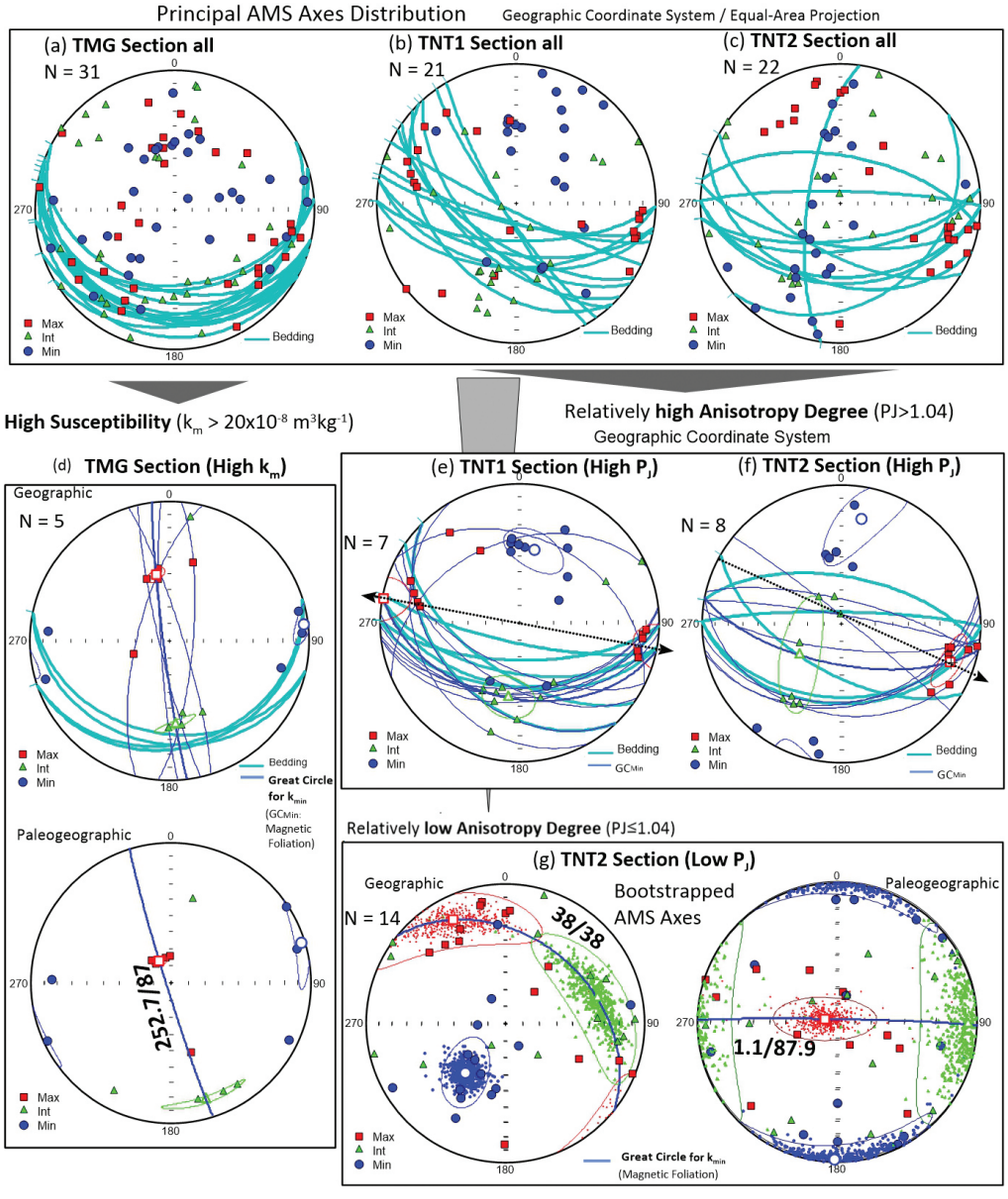

Fig. 10: (a-c): Stereograms of In Situ principal AMS axes with bedding planes at the level of specimens (N) from three sections in Jomsom area. TMG (Tamba Kurkur Formation); TNT1 and TNT2 (Upper Mukut Formation). (d-g): Magnetic fabric patterns (MFPs) discriminated by specific ranges of AMS parameters (bulk susceptibility, anisotropy degree and ellipsoid shape). The mean tensor and confidence ellipses are shown when the principal axes are relatively well-defined.

foliation shown by MFP2 seems to be subparallel to bedding or S2 (linked to the D2 deformation phase). Likewise, judging from sub-parallelism between the magnetic foliation and mean S4 (crenulation cleavage), MFP3 may be linked to the D4 deformation phase.

DISCUSSION

Multicomponent remanence

This study reconfirmed the multicomponent remanence (comprising the recent field, secondary, and primary components, with overlapping and distributed unblocking temperatures or coercivity spectra) in Triassic carbonates from Jomsom suggested by Klootwijk and Bingham (1980). Rockmagnetic experiments identified goethite and pyrrhotite to be the prominent secondary remanence carriers (Crouzet et al. 2003; Appel et al. 2012). Presence of component B (related to collision) and remagnetization circles caused by normal and reverse polarity directional pairs suggested by Kootwijk and Bingham (1980) could not be ascertained.

Acquisition of pyrrhotite remanence inferred at ca. 30 Ma or later following the major folding yielded a mean inclination steeper than the expected inclination (I_{exp}) by a maximum amount of 23.2° (section 4.2.3a). In analogy with previous works, this amount may be attributed to several different factors such as the regional-scale 'ramping of Tethys Himalaya on the Main Central Thrust (MCT)' (e.g., Appel et al. (1991) in Manang and Crouzet et al. (2001) in Hidden Valley or the medium-scale effects of 'crustal doming' resulting in the location-dependent 'tilting in different directions and with different angles' (e.g., Schill et al. 2003) in Nar Phu area. In the absence of details on structures at regional to local scale, and the structural complexity of the study area (Suzuki et al. 2010), the details of tilting can't be explained. A modelling exercise involving multidisciplinary dataset (geothermometers-based data, radiochronology, exhumation-related parameters (e.g., uplift/erosion rates, geothermal gradients, overburden thickness), remanence acquisition mechanisms etc. seems necessary to better constrain the age of such regionally pervasive and consistent ChRMpyr acquisition. Also, the spatial and temporal differences and causes between the steeper (ca. 60°, normal polarity) post-folding ChRMpyr (in Manang, Nar-Phu, Hidden Valley, Jomsom) and much shallower (ca. 30°, reverse polarity) and post-folding CHRMpyr recovered from similar formations in at least two adjacent areas (Dolpo and Shiar) require further attention.

Tethyan carbonates from Himalaya and Tibet are occasionally questioned as recorders of primary remanence due to the possible degree of severe remagnetization during the passage of exposure to several tectono-metamorphic events that followed the initial deposition and diagenesis. Debate continues among research groups reporting rockmagnetic and petrographic observations, in varying degree, in favor of the pervasive remagnetization (e.g., Huang et al., 2017 and 2019) or against (Yi et al., 2017; Zhao et al. 2021). The issue seems to continue as the low concentration and extremely fine size of magnetic minerals restrict their accurate identification: (i) with optical microscope; (ii) with commonly employed scanning electron microscopy aided with EDS that enables determining Fe and O but not the minerals (i.e., difficulty to discriminate hematite or magnetite, and to determine the state of oxidation); and (iii) by most magnetomineralogical experiments (e.g., IRM, thermomagnetic curves) that provide only indirect evidences for types and phases of magnetic minerals.

The Triassic marine sediments near Jomsom reflect the characteristics of weathered source rocks and effects related to fluvial transportation and depositional environments. So, initial detritus was prone to varying degree of modification by multiple factors such as climate, selective sorting in fluvial and marine processes, diagenesis, and metamorphism. The rocks studied lack in horizons with specific chemical composition or formation of authigenic mineral assemblages except for some authigenic dolomite, metamorphic mica minerals, and opaque grains, under microscope. Scanning probe measurement on sample TMG11 hinted to the presence of Ni-sulfides, but no clear signs of occurrence of authigenic Fe-bearing minerals such as magnetite. Radiometric data indicate a relatively weak metamorphism, equivalent to a strong diagenetic overprint attesting to detrital inheritance with only weak post-depositional heating (Bordet et al. 1971, p. 191). Thermochronometers-based data (section 2.2, above), support a maximum reheating range of 250-275°C. Magnetite-based characteristic remanence from the TMG section combined with Component C from two sections in Klootwijk and Bingham (1980) results in better grouping in support for acquisition prior to folding (section 4.2.3b). Taken together, these remanences are consistent with primary depositional magnetization acquired at southern hemisphere (about 34.5°S to 25°S) during the Triassic (251.9-208.5 Ma). Therefore, the newly determined ChRMmag serves as the evidence of preservation of primary magnetization in the Tethys Himalaya in Nepal and complements the existing paleomagnetic database.

Magnetic susceptibility and superposed magnetic fabric

In a recent AMS study of the rocks mainly from the Greater Himalaya Sequence but partially also overlying Tethys Himalayan and underlying Lesser Himalayan formations, magnetic fabric was discriminated into three classes characterized by the predominance of diamagnetic minerals (P_J>1.15, km<20 μSI), paramagnetic phyllosilicates (P_J<1.15, 20 μSI < k_m <100 μSI), and ferromagnetic minerals (P_J>1.15, km>100 μSI) (Parsons et al. 2016). Carbonates from the Tethys Himalaya measured in this study exhibit low bulk susceptibility magnitudes (k_m<20×10^{-8}m^{3}kg^{-1} (ca. 500 μSI)) except for a few TMG specimens (k_m range of (20-30) ×10^{-8}m^{3}kg^{-1}), while the maximum measured degree of anisotropy P_J never exceeds 1.12. Also, a positive relationship of P_J with k_m (and occasionally also with T) is evident when the former exceeds the value of P_J as low as 1.03. Therefore, this study adapted a P_J threshold of ca. 1.03 combined with k_m ranges (specific to sections) to create data subsets for subsequent analysis/visualization of magnetic fabric patterns and correlate them to the microstuctural elements observed macroscopically in the field commonly in lithologies other than the carbonate rocks and reported in the published literature. To be specific, the co-existence of three distinct patterns (section 5.3 above and Fig. 10) tentatively correlatable to the deformation structures within the structural 'domain 5' in Godin (2003) has been suggested. Alignments of all types of mineral types (ferromagnetic, paramagnetic and diamagnetic minerals) in varying proportions contribute to the observed superposed fabric.

AMS parameters in carbonates from the lower half of TNT1 section showed systematic variability (section 5.2 and Fig. 9) inferred to reflect the 'strain trajectory' related to subtle but gradual increase in deformation with burial depth (Pares 2004). Systematic observations on the microscopic structural fabric in these carbonates are yet to be made. Under microscope, the gray to black mudstones (ranging in lithology from claystone to coarse siltstone) intercalated with limestones of the Tamba Kurkur Formation exhibit signs of weak metamorphism. The mudstones occasionally include small (2–5 mm in diameter) burrows, and the quartzose and the feldspathic grains are predominantly angular to subangular. Recrystallization and weak deformation make their graded bedding obscure, and lead to distortion in the shapes of the biogenic and calcareous spherules. Limited thin section and scanning electron microprobe (SEM) observations on these samples do not provide clues to the magnetic fabric patterns revealed by the AMS anisotropy. So, it is desirable for any future AMS study in the Tethys realm to consider sampling several distinct lithologies for laboratory processing, collection of mesoscopic observations on structural elements in the field, and inclusion of laboratory observations to reveal the microscopic structures.

CONCLUSIONS

Carbonates of Triassic age (Tamba Kurkur and Mukut Formations) from three new sections yield secondary thermochemical remanence residing in pyrrhotite and acquired at <30 Ma following the major folding event. The rocks from Tamba Kurkur Formation additionally yield a primary depositional remanence residing in magnetite and acquired at intermediate latitude (35°S) in the southern hemisphere. The remanent magnetization components recovered are consistent with those reported earlier from carbonates from Jomsom and adjacent areas within the Dolpo-Manang Synclinorium and beyond (Shiar, Larkya, Nar-Phu, Hidden Valley) and therefore complement the existing paleomagnetic data.

The Triassic carbonates from Jomsom area exhibit low bulk magnetic susceptibility magnitudes (k_m <30×10^{-8} m^3kg^{-1}) contributed mainly by diamagnetic and paramagnetic minerals. Magnetic fabric based on the anisotropy of magnetic susceptibility reveals a low degree of anisotropy (P_J < 1.12) with both prolate and oblate susceptibility ellipsoids. However, a positive relationship of P_J with k_m (and occasionally also with T) is evident, when P_J exceeds ca. 1.03. The magnetic fabric is composite of 3-4 patterns defined by principal AMS axes and decipherable through analysis of subsets with specific ranges of AMS parameters (k_m, P_J and T). Some of these patterns can be correlated with the mesoscopic structures in the field, while others related to very weak deformation process may be uniquely revealed only by the AMS technique. Further magnetic fabric studies involving a variety of lithologies coupled with simultaneous collection of data on mesoscopic structures, to enable mutual comparison of magnetic fabric and petrofabric elements, are desirable.

ACKNOWLEDGEMENTS

This study was funded by a MEXT/JSPS KAKENHI-PROJECT-19403012 (PI: K. Yoshida). We express our gratitude to Y. Yamamoto and H. Machiyama for providing us expert guidance on equipment usage and data acquisition as well as making other necessary arrangements during the measurements at the palaeomagnetic laboratory in the Kochi Core Center, Japan.

REFERENCES

Acton, G.D., 1999, Apparent polar wander of India since the Cretaceous with implications for regional tectonics and true polar wander. Memoirs of the Geological Society of India, 44, pp. 129–175.

Aikman, A., Harrison, T.M. and Lin, D., 2008, Evidence for early (>44 Ma) Himalayan crustal thickening, Tethyan Himalaya, southeastern Tibet. Earth and Planetary Science Letters, 274, pp. 14–23.

Appel, E., Müller, R. and Widder, R.W., 1991, Palaeomagnetic results from the Tibetan Sedimentary Series of the Manang area (north central Nepal). Geophysical Journal International, 104 (2), pp. 255–266.

Appel, E., Schill, E. and Crouzet, C., 2012, Pyrrhotite remagnetizations in the Himalaya: a review. Geological Society, London, Special Publications, 371 (1): 163. https://doi.org/10.1144/sp371.1

Besse, J. and Courtillot, V., 1991, Revised and Synthetic Apparent Polar Wander Paths of the African, Eurasian, North American and Indian Plates, and True Polar Wander Since 200 Ma. Journal of Geophysical Research, 96, pp. 4029-4050.

Bordet, P., Colchen, M., Krummenacher, D., Le Fort, P., Mouterde, R. and Rémi, M., 1971, Recherches géologiques dans l'Himalaya du Népal, région de la Thakkhola. Centre National de la Recherche Scientifique, Paris, 279 pp (with two geological maps in colors)

Burg, J.P. and Chen, G.M., 1984, Tectonics and structural zonation of southern Tibet, China. Nature, 311, pp. 219–223.

Calvín, P., Villalaín, J.J. and Casas-Sainz, A.M., 2018, The carriers of AMS in remagnetized carbonates. Insights for remagnetization mechanism and basin evolution. Physics of the Earth and Planetary Interiors, 282, pp. 1-20. https://doi.org/10.1016/j.pepi.2018.06.003

Carosi, R., Montomoli, C. and Visona, D., 2007, A structural transect in the lower Dolpo: insights on the tectonic evolution of Western Nepal. Journal of Asian Earth Sciences, 29, pp. 407–423. https://doi.org/10.1016/j.jseaes.2006.05.001

Chadima, M., 2018, Anisoft - Advanced treatment of magnetic anisotropy data. EGU General Assembly Conference Abstracts, 15017.

Colchen, M., Le Fort, P. and Pecher, A., 1986, Annapurna, Manaslu, Ganesh Himal, C.N.R.S., Paris, pp. 1-136.

Coleman, M.E., 1996, Orogen-parallel and orogen-perpendicular extension in the central Nepalese Himalayas. Geological Society of America Bulletin, 108, pp. 1594–1607.

Crerar, D.A., Susak, N.J., Borcsik, M., and Schwartz, S., 1978, Solubility of the buffer assemblage pyrite + pyrrhotite + magnetite in NaCl solutions from 200 to 350 degrees C. Geochimica Cosmochimica Acta, 42, pp. 1427-1438.

Crouzet, C., Dunkl, I., Paudel, L., Arkai, P., Rainer, T.M., Balogh, K. and Appel, E., 2007, Temperature and age constraints on the metamorphism of Tethyan Himalaya in Central Nepal: a multidisciplinary approach. Journal of Asian Earth Sciences, 30, pp. 113–130.

Crouzet, C., Gautam, P., Schill, E. and Appel, E., 2003, Multicomponent magnetization in western Dolpo (Tethyan Himalaya, Nepal): tectonic implications. Tectonophysics, 377 (1-2), pp. 179-196.

Crouzet, C., Stang, H., Appel, E., Schill, E. and Gautam, P., 2001, Detailed analysis of successive pTRMs carried by pyrrhotite in Himalayan metacarbonates: an example from Hidden Valley, Central Nepal. Geophysical Journal International, 146, pp. 607–618.

Dhital, M.R., 2015, Geology of the Nepal Himalaya: Regional Perspective of the Classic Collided Orogen. Springer.

Dunlop, D.J. and Özdemir, Ö., 1997, Rock Magnetism. Fundamentals and Frontiers. Cambridge Studies in Magnetism Series. xxi + 573 pp. Cambridge University Press.

Fuchs, G., 1973, On the Geology of the Karnali and Dolpo Regions, West Nepal. Austrian Journal of Earth Sciences, 66-67, pp. 21-32.

Fuchs, G., 1977, The geology of the Karnali and Dolpo regions, western Nepal. Jahrb. Geol. Bundesanst, 120, pp. 165-217.

Garzanti, E., Gorza, M., Martellini, L. and Nicora, A., 1994a, Transition from diagenesis to metamorphism in the Paleozoic to Mesozoic succession of the Dolpo Manang synclinorium and Thakkola Graben (Nepal Tethys Himalaya). Eclogae Geologicae Helvetiae, 87, pp. 613–632.

Garzanti, E., Nicora, A. and Tintori, A., 1992, Late Paleozoic to Early Mesozoic stratigraphy and sedimentary evolution of central Dolpo (Nepal Himalaya). Riv. It. Paleont. Strat., 98, pp. 271-298.

Garzanti, E., Nicora, A. and Tintori, A., 1994b, Triassic stratigraphy and sedimentary evolution of the Annapurna Tethys Himalaya (Manang area, Central Nepal). Riv. It. Paleont. Strat., 100, pp. 195-226.

Gautam, P., Ulak, P.D., Paudayal, K.N., Gyawali, B.R. and Bhandari, S., 2012, Magnetostratigraphic dating of the prime-time sedimentary record of Himalayan tectonics and climate: new age constraints (13–10 Ma) from the Siwaliks of the Tinau Khola north section, Nepal. Geophysical Journal International, 190, pp.1378–1392.

Godin, L., 2003, Structural evolution of the Tethyan sedimentary sequence in the Annapurna area, central Nepal Himalaya. Journal of Asian Earth Sciences, 22, pp. 307–328.

Godin, L., Grujic, D., Law, R.D. and Searle M.P., 2006, Channel flow, ductile extrusion and exhumation in continental collision zones: An introduction, in Law, R.D., Searle, M.P. Godin, L., eds., Channel Flow, Ductile Extrusion and Exhumation in Continental Collision Zones: Geological Society of London Special Publication, 268, pp. 1–23. https://doi.org/10.1144/GSL.SP.2006.268.01.01

Gradstein, F.M., Gibling, M.R., Jansa, L.F., Kaminski, M.A., Ogg, J.G., Sarti, M., Thurow, J.W., Von Rad, U. and Westermann, G.E.G., 1989, Mesozoic stratigraphy of Thakkhola, central Nepal, Spec. Rep, 1. Centre for Marine Geology, Dalhousie Univ., Halifax, pp. 1–115.

Gradstein, F.M., Gibling, M.R., Sarti, M., Von Rad, U., Thurow, J.W., Ogg, J.G., Jansa, L.F., Kaminski, M.A., Westermann, G.E.G., 1991, Mesozoic Tethyan strata of Thakkhola, Nepal: evidence for the drift and breakup of Gondwana. Palaeogeography Palaeoclimatology Palaeoecology, 88, pp. 193–218.

Hagen, T., 1969, Report on the geological survey of Nepal. Volume 1: Preliminary Reconnaissance. Denkschiiften der Schweizerischen Naturforschenden Gesellschaft, Band LXXXVI/1, 185 pp.

Hatakeyama, T., 2018, Online plotting applications for paleomagnetic and rock magnetic data. Earth Planets and Space, 70:139. https://doi.org/10.1186/s40623-018-0906-5

Hodges, K.V., 2000, Tectonics of the Himalaya and southern Tibet from two perspectives. Geological Society of America Bulletin, 112(3), pp. 324-350.

Huang, W., Jackson, M.J., Dekkers, M.J., Zhang, Y., Zhang, B. and Guo, Z., 2019, Challenges in isolating primary remanent magnetization from Tethyan carbonate rocks on the Tibetan Plateau: Insight from remagnetized Upper Triassic limestones in the Eastern Qiangtang Block. Earth and Planetary Science Letters, 523, 115695. https://doi.org/10.1016/j.epsl.2019.06.035

Huang, W., Lippert, P.C., Zhang, Y., Jackson, M.J., Dekkers, M.J., Li, J., Hu, X., Zhang, B., Guo, Z., and van Hinsbergen, D.J.J., 2017, Remagnetization of carbonate rocks in southern Tibet: Perspectives from rock magnetic and petrographic investigations, Journal of Geophysical Research Solid Earth, 122. https://doi.org/10.1002/2017JB013987

Jelinek, V., 1981, Characterization of the magnetic fabric of rocks. Tectonophysics, 79, T63-67.

Kellett, D.A. and Godin, L., 2009, Pre-Miocene deformation of the Himalayan superstructure, Hidden valley, central Nepal. Journal of the Geological Society, London, 166, pp. 261–275.

Kirschvink, J.L., 1980, The least-squares line and plane and the analysis of palaeomagnetic data. Geophysical Journal of the Royal Astronomical Society, 62(3), pp. 699-718.

Klootwijk, C.T. and Bingham, D.K., 1980, The extent of greater India, III. Palaeomagnetic data from the Tibetan Sedimentary series, Thakkhola region, Nepal Himalaya. Earth and Planetary Science Letters, 51(2), pp. 381-405.

Kruiver, P.P., Dekkers, M.J. and Heslop, D., 2001, Quantification of magnetic coercivity components by the analysis of acquisition curves of isothermal remanent magnetization. Earth and Planetary Science Letters, 189, pp. 269–276.

Krystyn, L., 1982, Obertriassische Ammonoideen aus dem Zentralnepalesischen Himalaya. Abh. Geol. Bundesanst., 36, pp. 1-63.

Lascu, I., Banerjee, S.K. and Berquó, T.S., 2010, Quantifying the concentration of ferrimagnetic particles in sediments using rock magnetic methods. Geochemistry, Geophysics, Geosystems, 11, Q08Z19. https://doi.org/10.1029/2010GC003182

Liu, Q., Deng, C., Yu, Y., Torrent, J.M., Jackson, J., Banerjee, S.K. and Zhu, R., 2005, Temperature dependence of magnetic susceptibility in an argon environment: Implications for pedogenesis of Chinese loess/palaeosols. Geophysical Journal International, 161(1), pp. 102–112.

Lurcock, P.C. and Wilson, G.S., 2012, PuffinPlot: A versatile, user-friendly program for paleomagnetic analysis. Geochemistry, Geophysics, Geosystems, 13, Q06Z45. https://doi.org/10.1029/2012GC004098

Montomoli, C., Iaccarino, S., Carosi, R., Langone, A.D. and Visonà, D., 2008, Tectonometamorphic discontinuities within the Greater Himalayan Sequence in Western Nepal (Central Himalaya): Insights on the exhumation of crystalline rocks. Tectonophysics, 608, pp. 1349-1370.

Ogg, J.G. and Von Rad, U., 1994, The Triassic of the Thakkhola (Nepal). II. Paleolatitudes and comparison with other eastern Tethyan margins of Gondwana. Geologische Rundschau, 40(83), pp. 107-129.

O'Reilly, W., 1984, Rock and Mineral Magnetism. Blackie.

Pares, J.M., 2004, How deformed are weakly deformed mudrocks? Insights from magnetic anisotropy, In: Magnetic fabrics: Methods and applications (ed. Martín-Hernández F.). Geological Society special publication, 238, pp. 192-203.

Parsons, A.J., Ferré, E.C., Law, R.D., Lloyd, G.E., Phillips, R.J. and Searle, M.P., 2016, Orogen-parallel deformation of the Himalayan midcrust: Insights from structural and magnetic fabric analyses of the Greater Himalayan Sequence, Annapurna-Dhaulagiri Himalaya, central Nepal. Tectonics, 35, pp. 2515–2537. https://doi.org/10.1002/2016TC004244

Peters, C. and Dekkers, M.J., 2003, Selected room temperature magnetic parameters as a function of mineralogy, concentration and grain size. Physics and Chemistry of the Earth, Parts A/B/C, 28(16–19), pp. 659-667.

Ratschbacher, L., Frisch, W., Liu, G. and Chen, C., 1994, Distributed deformation in southern and western Tibet during and after the India–Asia collision. Journal of Geophysical Research, 99, pp. 19917–19945.

Rochette, P., 1987, Magnetic susceptibility of the rock matrix related to magnetic fabric studies. Journal of Structural Geology, 9(8), pp. 1015-1020. https://doi.org/10.1016/0191-8141(87)90009-5

Schill, E., Appel, E. and Gautam, P., 2002a, Thermotectonic history of the Tethyan Himalayas deduced from palaeomagnetic record of metacarbonates from Central Nepal (Shiar Khola). Journal of Asian Earth Sciences, 20, pp. 203–210.

Schill, E., Appel, E. and Gautam, P., 2002b, Towards pyrrhotite/magnetite geothermometry in low-grade metamorphic carbonates of the Tethyan Himalayas (Shiar Khola, Central Nepal). Journal of Asian Earth Sciences, 20, pp. 195–201.

Schill, E., Appel, E., Crouzet, C., Gautam, P., Wehland, F. and Staiger, M., 2004, Oroclinal bending and regional significant clockwise rotations of the Himalayan arc – constraints from secondary pyrrhotite remanences. In: Sussman, A.J., and Weil, A.B. (eds), Orogenic Curvature: Integrating Paleomagnetic and Structural Analysis. Geological Society of America, Boulder, Special Paper 383, pp. 73–85.

Schill, E., Appel, E., Godin, L., Crouzet, C., Gautam, P. and Regmi, K.R., 2003, Record of deformation by secondary magnetic remanences and magnetic anisotropy in the Nar/Phu valley (central Himalaya). Tectonophysics, 377, pp. 197–209.

Schill, E., Crouzet, C., Gautam, P., Singh, V.K., and Appel, E., 2002c, Where did rotational shortening occur in the Himalaya? – Inferences from palaeomagnetic remagnetisations. Earth and Planetary Science Letters, 203, pp. 45–57.

Schwertmann, U., 1988, Occurrence and formation of iron oxides in various pedoenvironments, in J.W. Stucki et al. (Eds.), Iron in Soils and Clay Minerals, pp. 267–308.

Suzuki, S., Dhital, M.R., Yoshida, K., Kawamura, T., Regmi, A.D., Gyawali, B.R, Otomo, K., Yamanaka, A. and Yukawa, H., 2010, Folded structures of Tethyan sedimentary succession, Annapurna region, Nepal Himalaya. The Journal of the Geological Society of Japan 16(6), VII-VIII. https://doi.org/10.5575/geosoc.116.6.VII_VIII

Torsvik, T.H., Müller, R.D., Van der Voo, R., Steinberger, B. and Gaina, C., 2008, Global plate motion frames: toward a unified model. Reviews of Geophysics 46(3), RG3004. https://doi.org/10.1029/2007RG000227

Upreti, B.N., 1999, An overview of the stratigraphy and tectonics of the Nepal Himalaya. Journal of Asian Earth Sciences, 17(5–6), pp. 577–606.

Vaes, B., van Hinsbergen, D.J.J., van de Lagemaat, S.H.A., van der Wiel, E., Lom, N., Advokaat, E.L., Boschman, L.M., Gallo, L.C., Greve, A., Guilmette, C., Li, S.H., Lippert, P.C., Montheil, L., Qayyum, A. and Langereis, C.G., 2023, A global apparent polar wander path for the last 320 Ma calculated from site-level paleomagnetic data. Earth-Science Reviews, 245, 104547. https://doi.org/10.1016/j.earscirev.2023.104547

von Rad, U., Duerr, S.B., Ogg, J.G. and Wiedmann, J., 1994, The Triassic of the Thakkhola (Nepal). I: stratigraphy and paleoenvironment of a north-east Gondwana rifted margin. Geologische Rundschau, 83, pp. 76-106.

Weil, A.B. and Yonkee, A., 2009, Anisotropy of magnetic susceptibility in weakly deformed red beds from the Wyoming salient, Sevier thrust belt: Relations to layer-parallel shortening and orogenic curvature. Lithosphere, 1(4), pp. 235–256. https://doi.org/10.1130/L42.1

Yi, Z., Appel, E. and Huang, B., 2017, Comment on "Remagnetization of the Paleogene Tibetan Himalayan carbonate rocks in the Gamba area: Implications for reconstructing the lower plate in the India-Asia collision" by Huang et al., Journal of Geophysical Research Solid Earth, 122. https://doi.org/10.1002/2017JB014353

Yin, A., 2006, Cenozoic tectonic evolution of the Himalayan orogen as constrained by along-strike variation of structural geometry, exhumation history, and foreland sedimentation. Earth Science Reviews, 76, pp. 1-131.

Yoshida, K., Kawamura, T., Suzuki, S., Regmi, A.D., Gyawali, B.R., Shiga, Y., Adachi, Y. and Dhital, M.R., 2014, Continental weathering in the Early Triassic in Himalayan Tethys, central Nepal: Implications for abrupt environmental change on the northern margin of Gondwanaland. Journal of Asian Earth Sciences, 79, Part A, pp. 288-301. https://doi.org/10.1016/j.jseaes.2013.09.011

Zhao, Q., Huang, B., Yi, Z. and Xue, P., 2021, High-resolution petrographic evidence confirming detrital and biogenic magnetites as remanence carriers for Zongpu carbonates in the Gamba Area, south Tibet. Frontiers in Earth Sciences, 9:713469. https://doi.org/10.3389/feart.2021.713469